HHS Public Access

Author manuscript

J Am Chem Soc. Author manuscript; available in PMC 2020 November 06.

Published in final edited form as:

J Am Chem Soc. 2019 November 06; 141(44): 17533–17547. doi:10.1021/jacs.9b05274.

Activation of Dioxygen by a Mononuclear Nonheme Iron Complex: Sequential Peroxo, Oxo, and Hydroxo Intermediates

Jesse B. Gordon[†], **Avery C. Vilbert**[‡], **Ida M. DiMucci**[‡], **Samantha N. MacMillan**[‡], **Kyle M. Lancaster**[*,‡], **Pierre Moänne-Loccoz**[*,§], **David P. Goldberg**[*,†]

[†]Department of Chemistry, The Johns Hopkins University, 3400 North Charles Street, Baltimore, Maryland 21218, United States

[‡]Department of Chemistry and Chemical Biology, Baker Laboratory, Cornell University, Ithaca, New York 14853, United States

[§]Department of Chemical Physiology and Biochemistry, Oregon Health & Science University, Portland, Oregon 97239, United States

Abstract

The activation of dioxygen by $Fe^{II}(Me_3TACN)(S_2SiMe_2)$ (**1**) is reported. Reaction of **1** with O_2 at −135 °C in 2-MeTHF generates a thiolate-ligated (peroxo)diiron complex $Fe^{III}_2(O_2)(Me_3TACN)_2(S_2SiMe_2)_2$ (**2**) that was characterized by UV–vis (λ_{max} = 300, 390, 530, 723 nm), Mössbauer (δ = 0.53, $|\Delta E_Q|$ = 0.76 mm s^{-1}), resonance Raman (RR) (ν(O–O) = 849 cm^{-1}), and X-ray absorption (XAS) spectroscopies. Complex **2** is distinct from the outer-sphere oxidation product $\mathbf{1^{ox}}$ (UV–vis (λ_{max} = 435, 520, 600 nm), Mössbauer (δ = 0.45, ΔE_Q = 3.6 mm s^{-1}), and EPR (S = 5/2, $\boldsymbol{g}$ = [6.38, 5.53, 1.99])), obtained by one-electron oxidation of **1**. Cleavage of the peroxo O–O bond can be initiated either photochemically or thermally to produce a new species assigned as an Fe^{IV}(O) complex, $Fe^{IV}(O)(Me_3TACN)(S_2SiMe_2)$ (**3**), which was identified by UV–vis (λ_{max} = 385, 460, 890 nm), Mössbauer (δ = 0.21, $|\Delta E_Q|$ = 1.57 mm s^{-1}), RR ($\nu(Fe^{IV}{=}O)$ = 735 cm^{-1}), and X-ray absorption spectroscopies, as well as reactivity patterns. Reaction of **3** at low temperature with H atom donors gives a new species, $Fe^{III}(OH)(Me_3TACN)(S_2SiMe_2)$ (**4**). Complex **4** was independently synthesized from **1** by the stoichiometric addition of a one-electron oxidant and a hydroxide source. This work provides a rare example of dioxygen activation at a mononuclear nonheme iron(II) complex that produces both Fe^{III}–O–O–Fe^{III} and Fe^{IV}(O) species in the same reaction with O_2. It also demonstrates the feasibility of forming Fe/O_2 intermediates with strongly donating sulfur ligands while avoiding immediate sulfur oxidation.

Graphical Abstract:

[*]**Corresponding Authors:** dpg@jhu.edu, kml236@cornell.edu, moennelo@ohsu.edu.

Supporting Information

The Supporting Information is available free of charge on the ACS Publications website at DOI: 10.1021/jacs.9b05274.

^{1}H NMR, EPR UV–vis, and Mössbauer spectra, cyclic voltammetry data, EXAFS data, EPR spectroscopy data, computational details, and DFT coordinates (PDF)

The authors declare no competing financial interest.

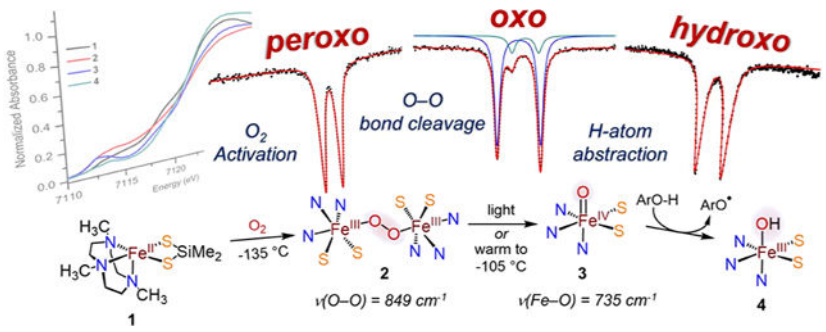

INTRODUCTION

The binding and activation of dioxygen by nonheme metal complexes has been the focus of major research efforts. Criteria for the design of complexes for O_2 activation include lowering the metal redox potential to a range suitable for reduction of O_2, and maintaining an open or labile site on the metal center for O_2 coordination.[1,2] A major motivation for designing such complexes comes from their potential to serve as catalysts for the selective oxidation of substrates,[3–6] as well as their ability to model key aspects of nonheme metalloenzyme structure and function.[1,7] Activation of O_2 by nonheme iron enzymes is proposed in many cases to involve three basic steps: binding of O_2 to a ferrous center to give a formal $Fe^{III}(O_2^{\bullet-})$, bridging of the putative superoxide to another redox-active cofactor (e.g., α-ketoglutarate, sulfur, a second Fe^{II}), and homolytic O–O cleavage to give high-valent ferryl ($Fe^{IV}(O)$) species. Similar O_2 activation schemes have been proposed for synthetic transition metal complexes, and, in the case of iron, this type of O_2 activation pathway has been observed with porphyrins.[8–12] However, similar reactivity toward O_2, in which a mononuclear nonheme iron complex reacts with O_2 to give well-defined peroxo-bridged and high-valent oxo intermediates, to our knowledge, is still unknown.

A subset of O_2-activating nonheme iron enzymes relies on thiolate-ligated iron centers, including isopenicillin N synthase (IPNS),[13,14] the thiol dioxygenases,[15,16] such as cysteine dioxygenase (CDO), and the sulfoxide synthases,[17,18] EgtB and OvoA (Figure 1). The presence of sulfur in the first coordination sphere adds a level of complexity to the mechanism of O_2 activation, because sulfur is readily oxidized to produce a range of products (e.g., disulfide, S-oxygenates). The selective, controlled oxidation of the sulfur centers is often an essential step for these enzymes.

Developing a fundamental understanding of how Fe activates O_2, particularly in the presence of thiolate donors, and spectroscopically identifying the succeeding Fe/O_2 intermediates is central to determining how nonheme thiolate-ligated iron metalloenzymes function. Despite these enzymes having thiolate donors cis to the proposed O_2 binding sites, the modes of O_2 activation and subsequent substrate oxidation by these oxidase and oxygenase enzymes differ dramatically. IPNS performs hydrogen atom abstractions from substrate C–H bonds,[19] whereas the thiol dioxygenases perform S-oxygenation,[20] and sulfoxide synthases perform both S-oxygenation and C–S bond coupling.[17,21,22] A central mechanistic question is how these enzymes catalyze their divergent reactivity with similar sulfur ligation. It is clear that

all of these enzymes must bind and activate O_2, and must cleave the O–O bond to perform their respective reactions. Difficulties trapping and identifying catalytically relevant O_2 intermediates in these enzymes have hampered the ability to delineate these mechanisms, and, as a result, determining the origin of the discriminate reactivity is challenging.

Our laboratory[23–27] and others[28–34] have made considerable efforts to construct sulfur-ligated iron complexes that can activate O_2, to examine aspects of structure and function. A major emphasis has been to trap and characterize the Fe/oxygen intermediates following reaction of Fe^{II} with O_2, to determine their chemical reactivity and spectroscopic properties, and compare these properties with proposed enzymatic intermediates. Well-defined, iron–oxygen adducts derived from synthetic nonheme Fe^{II} complexes and O_2 are uncommon. The anticipated initial intermediate, an Fe^{III}(superoxo) species, was not characterized in a mononuclear nonheme Fe complex until 2014–2015,[35,36] and the first thiolate-ligated Fe^{III}(superoxo) species were reported in 2018–2019.[29,33] There are several examples of well-defined diferric, peroxo-bridged complexes obtained from nonheme Fe^{II}/O_2, but none that involve sulfur ligation.[37] Only one example of a nonheme, sulfur-ligated Fe^{IV}(O) complex has been reported, and was prepared from the O atom donor *meta*-chloroperbenzoic acid, not O_2.[38]

Our lab previously reported a combined enzyme/model study that utilized triazacyclononane (TACN) to synthesize iron analogues of the thiol dioxygenases.[27] In a separate study, we demonstrated that the Co(TACN) complex $Co^{II}(Me_3TACN)(S_2SiMe_2)$ was capable of binding and activating O_2 to generate a Co(superoxo) species (Scheme 1).[39] The analogous Fe^{II} complex, $Fe^{II}(Me_3TACN)(S_2SiMe_2)$ (**1**), was previously reported and noted to be air-sensitive; however, the reactivity of **1** with O_2 was not examined in any detail.[40] Given our ability to stabilize a Co/O_2 intermediate using the same ligand set, we sought to examine the reactivity of **1** with O_2.

Here, we report the activation of dioxygen by $Fe^{II}(Me_3TACN)(S_2SiMe_2)$ to generate a thiolate-ligated diiron peroxo complex that can be stabilized at low temperature. This complex undergoes either thermolytic or photolytic O–O bond cleavage to generate a rare example of a thiolate-ligated Fe^{IV}(O) species. This Fe^{IV}(O) complex exhibits H atom abstraction reactivity, producing an Fe^{III}(OH) species. The generation, stability, and spectroscopic properties of these O_2-derived species are presented.

RESULTS AND DISCUSSION

Complex **1** was synthesized as previously reported and isolated as a colorless, crystalline solid.[40] In the original report, there was no description of UV–vis or Mössbauer spectroscopy for **1**. As expected, the UV–vis spectrum for colorless 1 in 2-MeTHF is featureless in the visible region (Figure S1), and exhibits a major peak in the UV region at 269 nm. The Mössbauer spectrum of solid **1** dispersed in boron nitride at 5 K exhibits an isomer shift (δ) of 0.92 mm s^{-1} and a quadrupole splitting ($|\Delta E_Q|$) of 2.27 mm s^{-1}, consistent with a high-spin Fe^{II} center (Figure S2). Electrochemical measurements by cyclic voltammetry (CV) reveal that **1** undergoes an initial, reversible oxidation at $E_{1/2} = -0.60$ V (versus Fc^+/Fc), and a second oxidation event at $E_{1/2} = 0.82$ V. These redox events can be

assigned to the formal $Fe^{III/II}$ and $Fe^{IV/III}$ couples, respectively. However, we have previously found that the analogous cobalt complex exhibits significant metal–ligand covalency with the silanedithiolate ligand, and redox transformations were assigned to the $[CoS_2]^+/[CoS_2]^0$ unit, as opposed to purely metal-based oxidation state changes.[39] The observation of two oxidations for **1** in Figure 2 contrasts the single redox event observed for $Co^{II}(Me_3TACN)(S_2SiMe_2)$, and is consistent with the ability of iron to access the formal +4 oxidation state. We and others have shown that a lower redox potential ($E_{1/2}(Fe^{III/II})$) favors facile reactivity with O_2,[2,24,41] and thus the first oxidation ($E_{1/2}$ = −0.60 V) for **1** suggested that it should react readily with O_2.

To examine if the first oxidation for **1** is chemically accessible, we reacted **1** with one-electron oxidants of appropriate strength. Addition of 1 equiv of the tetrakis-(pentafluorophenyl)borate salts of ferrocenium ($FcBAr^F{}_4$) or dimethylferrocenium ($^{Me2}FcBAr^F{}_4$) oxidants to **1** in 2-MeTHF at −80 °C results in the formation of new bands at 300, 435, 520, and 600 nm (Figure 3), corresponding to $\mathbf{1^{ox}}$. This species is thermally unstable and upon warming decays completely by −35 °C. Spectral titration of $^{Me2}FcBAr^F{}_4$ at −80 °C shows the expected 1:1 stoichiometry (Figure S5), and the reversibility of this oxidation was demonstrated by reverse titration with the one-electron reductant cobaltocene regenerating **1**, followed again by reoxidation back to $\mathbf{1^{ox}}$ with further addition of $^{Me2}FcBAr^F{}_4$ (Figure S7).

Because of the thermal instability of $\mathbf{1^{ox}}$, we have been unsuccessful at growing single crystals for X-ray diffraction (XRD). However, spectroscopic analyses together with DFT calculations were employed for further characterization of $\mathbf{1^{ox}}$ in situ. The EPR spectrum of $\mathbf{1^{ox}}$ at 20 K is shown in Figure 3, and is consistent with a high-spin ferric (S = 5/2) center, with $\boldsymbol{g}$ = [6.38, 5.53, 1.99], and an E/D = 0.016 from a simple rhombogram analysis.[42] Mössbauer spectroscopy of $\mathbf{1^{ox}}$ enriched in 57Fe (95.5%) in 2-MeTHF at 80 K reveals a quadrupole doublet with δ = 0.45 mm s^{-1} and $|\Delta E_Q|$ = 3.6 mm s^{-1} (Figure S8). The isomer shift is typical of Fe^{III} (S = 5/2) complexes.

Geometry optimizations by DFT of the one-electron oxidized, 5-coordinate $[Fe(Me_3TACN)(S_2SiMe_2)]^+$ and the THF-bound analogue, $[Fe(THF)(Me_3TACN)(S_2SiMe_2)]^+$, in the sextet state were carried out with the BP86/6–311g*/6–31g*(C,H) functional/basis set combination. The same level of theory was used to obtain an optimized structure for the starting material **1** in the quintet state, and this structure matched well with the structure from XRD,[40] helping to validate the theoretical methods. The optimized geometry for the oxidized species remained intact and gave metal–ligand distances that were slightly contracted, as expected for the oxidized complex. Calculation of the Mössbauer parameters[43] for **1** gave δ = 0.86 mm s^{-1} and $|\Delta E_Q|$ of 2.70 mm s^{-1}, which is a good match with experiment. The calculated parameters for $[Fe(Me_3TACN)(S_2SiMe_2)]^+$ are δ = 0.38 mm s^{-1}; $|\Delta E_Q|$ = 1.62 mm s^{-1}, and for $[Fe(THF)(Me_3TACN)(S_2SiMe_2)]^+$ are δ = 0.53 mm s^{-1}; $|\Delta E_Q|$ = 0.89 mm s^{-1}. In both cases, the quadrupole splitting is small as compared to the experimental value. However, the error in the calculation of the quadrupole splittings can be large, particularly for large values of $|\Delta E_Q|$.[44] The isomer shifts of the 5-coordinate and THF-bound structures are both close to the experimental isomer shift; therefore, at this time, we cannot conclusively rule out either structure.

Reactivity with O_2.

Addition of excess O_2 to a solution of **1** in THF at 23 °C leads to rapid color change from colorless to orange, followed by precipitation of dark brown solids and bleaching of the solution. These observations suggested oxidation to ferric ion followed by decomposition. However, the same reaction run in THF at −80 °C leads to a new color change to dark green, which converts to a pale orange color within seconds. Further cooling of the reaction to temperatures just above the freezing point of THF (−108 °C) led to a minor increase in the lifetime of the green intermediate, but rapid decay still occurred (Figure S9). Switching the solvent to 2-MeTHF allowed for further cooling to −135 °C, and we were pleased to find that the new green species (**2**) was thermally stabilized at this temperature, exhibiting bands at 300 ($\varepsilon \approx 9900$ M^{-1} cm^{-1} per Fe), 390 ($\varepsilon \approx 5000$ M^{-1} cm^{-1} per Fe), 530 ($\varepsilon \approx 2050$ M^{-1} cm^{-1} per Fe), and 723 ($\varepsilon \approx 3600$ M^{-1} cm^{-1} per Fe) nm (Figure 4). The reversibility of formation of **2** was tested by sparging the solution with Ar for 1 h or multiple vacuum/purge cycles, but no reversible oxygenation was observed. No evidence of significant decay of **2** is seen until the solution is warmed to −120 °C, which then results in further spectral changes (vide infra). These observations provided us with a temperature range for further spectroscopic analysis.

Reaction of **1** with excess O_2 for EPR spectroscopy was carried out directly in quartz EPR tubes cooled to −130 °C (pentane/N_2(l) bath). Upon formation of the green species **2**, the reaction mixture was frozen at 77 K, and it was noted that the dark green color quickly bleached to a light orange upon exposure to ambient light. This observation indicated **2** is highly photosensitive, even in frozen solution at 77 K, and thus all subsequent experiments were carried out in the dark. The EPR spectrum of **2** was silent, suggestive of an integer-spin species. Isotopically enriched **2(**^{57}**Fe)** was prepared in 2-MeTHF, and analysis by Mössbauer spectroscopy at 80 K revealed a single, sharp quadrupole doublet with δ of 0.53 mm s^{-1} and $|\Delta E_Q|$ of 0.76 mm s^{-1} (Figure 5). These parameters are typical of high-spin ($S = 5/2$) iron(III).[45] The same quadrupole doublet is observed at 5 K, even in the presence of a 50 mT magnetic field (Figures S10 and S11), indicating the absence of magnetic hyperfine splitting, and consistent with an integer-spin species.

Green **2** was examined further with resonance Raman (RR) spectroscopy. The extreme photosensitivity of **2** led to difficulties in this vibrational characterization because laser irradiation at 647, 514.5, or 407 nm invariably led to rapid and irreversible photobleaching, even at low laser power and with rapid sample spinning. However, short data acquisition with the 407 nm laser excitation could be averaged over multiple sets of samples to successfully identify RR signals attributable to **2** (Figure 6). Specifically, comparing averages of the first 30 s data accumulation and of the subsequent 30 s data isolates a RR signal at 849 cm^{-1} from the rich Raman spectrum of the solvent 2-MeTHF. Using the same procedure with samples prepared with $^{18}O_2$ allows isolation of a RR band at 802 cm^{-1}, which corresponds to a −47 cm^{-1} downshift that matches expectation from Hooke's law for an O–O harmonic oscillator (calculated $\Delta^{18}O = -49$ cm^{-1}). This 849 cm^{-1} value is typical of an iron(III)-(hydro)peroxo complex.[46–49] Although the initial reaction between **1** and O_2 can be expected to yield an Fe^{III}(superoxo) species with ν(O–O) around 1200 cm^{-1},[50] there is no evidence for such species in the RR spectra. Instead, the ν(O–O) at 849 cm^{-1} is

consistent with the formation of a (peroxo)diiron complex, which likely forms immediately upon O_2 binding. Symmetric ν(Fe–O) vibrations are resonance enhanced in most bridging diferric-peroxo complexes, but no such mode is observed in the RR spectra of **2**, as seen in a few other diiron peroxo species.[51–55] The RR difference spectra reveal an additional photosensitive vibration at 314 cm^{-1}, but it does not display any significant sensitivity to ^{18}O-labeling and is thus tentatively assigned to a $\nu(Fe^{III}–S)$ stretch on the basis of prior assignment of Fe–S stretching vibrations in stable synthetic complexes and metalloproteins.[56–58] This overall analysis of the RR data in terms of a bridging diferric-peroxo structure is consistent with the EPR-silent character of **2** and magnetic coupling of the high-spin Fe(III) through the peroxo bridge.[37,59]

XAS Studies.

Further insight into the structure of **2** was obtained by X-ray absorption (XAS) spectroscopy. The Fe K-edge XAS spectra of **1** and **2** are shown in Figure 7. The position of the rising edge for **1** (7122.3 eV) is slightly red-shifted by 0.2 eV upon conversion to **2** (7122.1 eV). A broad pre-edge feature is also present in both species accompanied by a slight change in energy from 7114.8 eV (**1**) to 7114.6 eV (**2**).

Fitting of the EXAFS region for **1** (Figure S13 and Table S1) was accomplished with 3 N scatterers with Fe–N_{ave} = 2.28 Å, and 2 S scatterers with Fe–S_{ave} = 2.50 Å. The N distance is in good agreement with Fe–N_{ave} = 2.253(9) Å observed by single-crystal XRD. However, the average sulfur distance is elongated in comparison to the data from XRD (Fe–S = 2.371(2)–2.410(2) Å).[40] The EXAFS of **2** (Figure 8 and Table 1) is best fit with a six-coordinate Fe center, including three Fe–N scatterers at 2.17 Å, two Fe–S_{ave} = 2.68 Å, and one short Fe–O scatterer at 1.93 Å. The scatterer with the smallest *R* is assigned as the Fe–O(peroxo) bond and is a typical length for other end-on Fe(peroxo) complexes.[37] The Fe–S distance is elongated (relative to the calculated model, vide infra), although this appears to be attributed to a high degree of correlation between *R* for the Fe–S scatter and the global shift to E_0. This same correlation is observed in the fits to **1**. Likewise, the Fe–N_{ave} distance is also shorter than predicted by DFT, but *R* for this path is correlated to that for the Fe–O. Exclusion of any of the inner-sphere scattering paths (N, O, S) gave unphysical fitting Debye–Waller parameters for the remaining included paths.

The Fourier transform of the k = 2–12 $Å^{-1}$ EXAFS data reveals appreciable amplitude near 4 Å. This is far greater in magnitude than that seen in the EXAFS of **1** (Figure S13) and thus cannot merely be attributed to distal Fe–Si–S and Fe–S–N multiple scattering (MS). Adequate fits require inclusion of Fe–Fe and Fe–O–Fe MS paths. The value of *R* for the Fe–Fe path is moderately correlated to the Debye–Waller factor for the Fe–O–Fe MS path. Moreover, other MS paths are expected to contribute to this shell. Consequently, we elect to use these paths as a bracket on the Fe–Fe distance, affording a range of 4.4–4.75 Å.

Together, the vibrational, Mössbauer, EPR, and EXAFS data support formulation of **2** as a diiron peroxo species (Scheme 2). An Fe–Fe distance within the range 4.4–4.75 Å is longer than seen for other diiron peroxo complexes,[37] although in most of these other cases the diiron unit is bridged by one or more supporting ligands (e.g., OH^-, RCO_2^-). The Fe–Fe

distance range for **2** is comparable to the Co–Co distances in dicobalt, unsupported peroxo-bridged structures.[60–63]

Geometry optimization of **2** was accomplished using a BP86/6–311G*/6–31G*(C,H) functional/basis set combination using broken symmetry (BS) assuming coupling between the two $S = 5/2$ iron centers. Several models of the diiron peroxo complex were tested; however, the model that provided the best match with experiment was that with the thiolate donors in a gauche orientation with respect to the peroxo core. Broken symmetry models involving two $S = 3/2$ Fe centers were also tested and gave results similar to the $S = 5/2$ calculations. However, the intermediate spin state $S = 3/2$ is unusual for Fe^{III}, and we favor the $S = 5/2$ description for **2**.[37] The geometry optimization of **2** provided metrical parameters that matched reasonably well with those seen by EXAFS, with the exception of the Fe–S bonds, which optimize at shorter distances. However, the Fe–S distances from EXAFS are likely overestimated (vide supra). The calculations also predict an Fe–Fe distance of 4.61 Å, which is close to that obtained from the fit of the EXAFS data. A magnetic coupling constant J of $-5.5\ cm^{-1}$ is calculated, indicating antiferromagnetic coupling between the two Fe centers ($\hat{H} = -2J_{AB}\hat{S}_A \cdot \hat{S}_B$, see Experimental Section). The weak antiferromagnetic coupling is consistent with an unsupported peroxo(diiron) complex. Similar coupling constants have been obtained for other diiron peroxo complexes.[49,65,66] Vibrational frequency calculations predict ν(O–O) = $893\ cm^{-1}$, with a calculated downshift of $-50\ cm^{-1}$ for the ^{18}O isotopologue of **2**, which are both reasonably close to the experimental values. Mössbauer calculations give $\delta = 0.52\ mm\ s^{-1}$ and $|\Delta E_Q| = 0.83\ mm\ s^{-1}$, which is a close match with the experimental values.

Complex **2** appears unreactive toward either H atom donors (e.g., phenols, TEMPOH, 1,1-diphenylhydrazine (DPH)), or O atom acceptors (e.g., PMe_3, PPh_3, PhSMe). However, addition of lutidinium tetrafluoroborate ([LutH]BF_4), a weak proton donor (pK_a 7.2 in THF),[67] to **2** at −135 °C results in the formation of $\mathbf{1^{ox}}$ as seen by both EPR and UV–vis spectroscopies (Figure S14). Use of the weaker acid [Et_3NH]-BF_4 (pK_a 12.5 in THF),[67] however, results in only very minor decay over 1.5 h. These results are consistent with protonation and release of H_2O_2 from **2**. Attempts to measure the released H_2O_2 by standard analytical methods[68–71] were unsuccessful. However, these methods require warm up of the reaction mixture to ambient temperature, which likely results in consumption of H_2O_2 by reaction with the easily oxidized silanedithiolate ligand. Addition of H_2O_2 to $\mathbf{1^{ox}}$ at −135 °C results in no reaction; however, H_2O_2 could no longer be detected upon warmup of this reaction to 23 °C, supporting the hypothesis that H_2O_2 is consumed upon warmup.

O–O Bond Cleavage.

The photosensitivity of **2** motivated us to further examine decay of **2** in the presence of light. Illumination of **2** in 2-MeTHF at −135 °C with a 619 nm LED light source was monitored by UV–visible spectroscopy, and showed isosbestic conversion to a new species with bands at 385 ($\varepsilon \approx 2600\ M^{-1}\ cm^{-1}$), 460 ($\varepsilon \approx 1500\ M^{-1}\ cm^{-1}$), and 890 ($\varepsilon \approx 390\ M^{-1}\ cm^{-1}$) nm (Figure 9). This new species **3** is stable for at least 1 h in the absence of further illumination. Exposure of **3** to UV light (300 nm) leads to further change of the spectral features, indicating that **3** is also photosensitive (Figure S15). Illumination of a frozen glass of **2** at 77

K results in a color change from dark green to the pale orange of **3**, and subsequent EPR spectroscopy reveals that **3** is EPR silent. Similarly, exposure of frozen solution Mössbauer samples of **2** to 619 nm light at 77 K results in a new quadrupole doublet with $\delta = 0.21$ mm s^{-1} and $|\Delta E_Q| = 1.57$ mm s^{-1} (80% total fit) as the major component, and a minor quadrupole doublet with $\delta = 0.49$, $|\Delta E_Q| = 1.17$ mm s^{-1} (20% of the fit) (Figure 10). Further illumination with a UV lamp results in the disappearance of the major component over 30 min, and full formation of the minor species as seen by Mössbauer spectroscopy (Figure S16).

The long wavelength, relatively weak band seen for **3** at 890 nm in the UV–vis spectrum is characteristic of nonheme intermediate spin ($S = 1$) Fe^{IV}(O) species (Scheme 3).[72] The absence of an EPR signal at X-band for **3** is consistent with an integer-spin Fe^{IV}(O) complex. The relatively low isomer shift ($\delta = 0.21$ mm s^{-1}) seen for **3** in the Mössbauer spectrum is close to those observed for $S = 1$, alkylamine-ligated Fe^{IV}(O) species ([Fe^{IV}(O)(TMC)(X)]$^{2+}$ (X = CH_3CN, OTf, NCO, NCS, N_3, CN, OH); $\delta = 0.15$–0.20 mm s^{-1}),[72,73] including a thiolate-ligated example ([Fe^{IV}(O)(TMCS)]PF_6; $\delta = 0.19$ mm s^{-1}).[38] A plot of the wavelength of the low energy peak for a range of Fe^{IV}(O) ($S = 1$) complexes versus isomer shift reveals a linear correlation, and the isomer shift and UV–vis feature for **3** fit this observed trend (Figure S17).

Resonance Raman spectroscopy provided additional evidence for the formation of an Fe^{IV}(O) species. Specifically, RR spectra of **3** obtained with 351 nm excitation exhibit a strongly resonance enhanced band at 735 cm^{-1} that downshifts to 703 cm^{-1} when **3** is prepared with $^{18}O_2$ gas (Figure 11). This 32 cm^{-1} ^{18}O-downshift matches the calculated value for an isolated Fe–O harmonic oscillator. The ν(Fe=O) signal is only mildly photosensitive relative to the peroxo complex, but without sample spinning the 735 cm^{-1} band is bleached within minutes under the 351 nm laser illumination, as expected from the UV-induced absorption changes discussed above.

The ν(Fe=O) for **3** is, to our knowledge, the lowest reported thus far for an Fe^{IV}(O) complex,[74,75] but alternative assignments of **3** (e.g., ν(Fe^{III}–O) and ν(Fe^{IV}–OH))[76,77] do not fit the experimental data. Rather, the low ν(Fe=O) in **3** may arise from the highly electron-donating thiolate ligands, which can also behave as noninnocent, redox active ligands.[39] Thus, some Fe^{III}(O)(thiyl radical) character for **3** cannot be ruled out. Many Fe^{IV}(O) complexes characterized by RR contain neutral/monoanionic ligand sets and are thus expected to be significantly less activated. Although no vibrational data for the thiolate-ligated Fe^{IV}(O) complex [Fe^{IV}(O)(TMCS)]$^+$ have been reported, EXAFS analysis on this species indicates an Fe=O bond length of 1.70 Å,[38] which, according to a Badger's rule analysis,[78] would correspond to a ν(Fe=O) of 752 cm^{-1}. Similarly weak Fe^{IV}=O bonds were also observed for an Fe^{IV}(O) complex with a tetraamido ligand set (d(Fe–O) = 1.690 Å)[79] as well as compound II of horseradish peroxidase (d(Fe–O) = 1.70 Å).[80]

The structure of **3** was further scrutinized by Fe K-edge XAS (Figures 12 and 13, and Table 2). The spectrum exhibits an intense pre-edge feature at 7112.5 eV. Fe K-edge EXAFS were obtained to a k of 14.4 Å^{-1} and fitted to substantiate the presence of an oxo ligand. As encountered in fitting the EXAFS of **1** and **2**, data resolution led to a high degree of fit

parameter correlation between the Fe–N and Fe–S scattering paths. The inclusion of a short Fe–O path with R of 1.687(6) Å significantly improved the fit. A high Debye–Waller factor is found for this path if the Mössbauer-derived proportion of **3** was factored in to produce a Fe–O CN of 0.8. Although we recognize that the Debye–Waller and CN parameters are moderately correlated, a better fit with a more reasonable Debye–Waller factor was obtained when this CN was permitted to float to 0.57(7), which is reasonable given the ca. 20–25% error endemic to CN in EXAFS fitting.[64] Taken together, all of the spectroscopic data confirm the assignment of **3** as an $Fe^{IV}(O)$ complex, which can be generated either in fluid solution or in frozen matrix by illumination with a relatively weak light source.

Warming a solution of **2** from −135 to −105 °C in the dark also leads to the formation of **3**, as seen by UV–vis and Mössbauer spectroscopies. The quadrupole doublet of **3** under these conditions exhibits slightly different parameters from the photochemically generated **3**, which can be attributed to slight differences in the local environment when **3** is generated in fluid solution versus frozen matrix. It can be concluded that cleavage of the O–O bond of **2** occurs through either thermal or photochemical activation.

DFT calculations on **3** provided further insights. The experimental data could not distinguish the spin state of the ground state for **3**; therefore, geometry optimizations of the triplet and quartet ferryl structures were performed using the methods detailed above as well as several alternative methods. Calculations of **3** in the quintet state did not provide a good match with the experimental data. In each case in the $S = 1$ state, the geometry optimization underestimated the Fe–O bond length (calcd d(Fe–O) = 1.63–1.66 Å) from the EXAFS data (d(Fe–O) = 1.687 Å), and, as a result, the calculated ν(Fe–O) was overestimated. Underestimation of a metal–Oxo bond length by DFT was also observed for a recently reported $Co^{IV}(O)$ complex.[81] A geometry scan of the Fe–O bond length reveals a relatively flat surface potential, with the structure exhibiting d(Fe–O) = 1.7 Å being within 1 kcal mol $^{-1}$ in energy from the lowest energy structure (Figure S29). A constrained geometry optimization with an Fe–O distance fixed at 1.7 Å provided a suitable structure for **3** and a calculated ν(Fe–O) of 731 cm^{-1}, which is a close match with the experimental data. Subsequent Mössbauer calculations on the constrained structure gave calculated parameters of $\delta = 0.15$ and $|\Delta E_Q|$ of 1.66 mm s^{-1}, which are in good agreement with the experimental data. Single point calculations were performed using the B3LYP/ZORA-def2-TZVP(-f)/CP(PPP) (on Fe) functional/basis set combination, and predicts that a significant amount of spin density (0.6 spins) should be located on the O atom. Taken together, these data support the conclusion that **3** is a mononuclear, $Fe^{IV}(O)$ species obtained via cleavage of the O–O bond in **2**.

Reactivity of 3.

In contrast to **2**, complex **3** reacts with H atom donors. Addition of 4-methoxy-2,2,6,6-tetramethylpiperidin-1-ol (4-OMe-TEMPOH) results in the rapid decay of **3** and formation of a new species, **4**, with bands at 410 and 485 nm in the UV–vis spectrum. Similarly, addition of 2,6-di-*tert*-butyl-4-methoxyphenol (4-OMe-dtbp) or 2,4,6-tri-*tert*-butyl-phenol (ttbp) results in the disappearance of **3** and formation of the band at 485 nm, while the band at 410 nm is masked by a new, sharp peak at 409 nm, which corresponds to the phenoxyl

radical (Figure 14). The EPR spectrum of the reaction of **3** with 4-OMe-dtbp reveals a peak at $g = 4.3$ and a sharp, intense peak at $g = 2.004$, which is assigned to the anticipated Fe^{III} product and phenoxyl radical, respectively (Figure 14). Spin quantitation of the EPR signals reveals a >95% yield for the high-spin Fe^{III} species **4** and a 75% yield for the phenoxyl radical (average of three runs; see Supporting Information).

Mössbauer spectroscopy on the reaction of excess 4-OMedtbp and **3(**^{57}**Fe)** leads to complete disappearance of the quadrupole doublet for **3** and formation of a new, major species with $\delta = 0.49$ mm s^{-1}, $|\Delta E_Q| = 1.08$ mm s^{-1} (Figure 15). This new quadrupole doublet for **4** is typical of hs-Fe^{III}, consistent with the EPR data. Thus it is reasonable to conclude that **4** is the expected Fe^{III}(OH) product formed immediately after a single H-atom abstraction by **3** (Scheme 4).

Further support for the assignment of **4** as a mononuclear Fe^{III}(OH) complex comes from XAS. The spectrum obtained for **4** exhibits a pre-edge feature at 7113.6 eV with diminished intensity relative to the pre-edge feature encountered in the spectrum of **3** (Figure 12). The effectively invariant rising edge and pre-edge energies are reminiscent of a recent observation by Que and co-workers that Fe K-edge energies cannot be used to unambiguously assign Fe oxidation states.[82] This diminished intensity is consistent with elongation of the Fe–O bond that would occur following hydrogen atom transfer (HAT). This result is supported by the EXAFS of **4** (Figure 16 and Table 3), which is best fit with a six-coordinate Fe center with three Fe–N scatterers at 2.25 Å, two Fe–S_{ave} = 2.39 Å, and one Fe–O scatterer at 1.91 Å. The Fe–O scatterer is assigned to the Fe–OH bond, and has a bond length similar to that of other mononuclear ferric hydroxide species.[82–84]

DFT studies were performed to corroborate the experimental data. Geometry optimization of **4** gives bond metrics that are in good agreement with the EXAFS-derived bond distances. Calculation of the Mössbauer parameters gives $\delta = 0.44$, $|\Delta E_Q| = 0.77$ mm s^{-1}, which are also a good match with the experimental data. Additional evidence for assignment of **4** comes from mixing Bu_4NOH or LiOH (1 equiv) with the oxidized $\mathbf{1^{ox}}$, which leads to the formation of **4** as seen by both UV–vis and Mössbauer spectroscopy (Figures S26–S28). The Mössbauer spectrum in Figure 15 for the HAT product is slightly broader than the spectrum seen for the LiOH product. This broadness may be due to the presence of the ~20% photodecay product from the ferryl species seen in Figure 10, which has Mössbauer parameters nearly identical to those of **4**. These data are consistent with complex **3** being able to perform a single H-atom abstraction with phenols to generate a mononuclear ferric hydroxide species.

Complex **3**, however, is unreactive toward weak C–H bond substrates such as xanthene, acridine, and *N*-benzyldihydronicotinamide. The differences in reactivity between O–H and C–H bonds with comparable bond strengths are well-established and have been discussed previously.[85] In addition, **3** is unreactive toward OAT reactions, as no reaction is observed with thioanisole, PPh_3, or PMe_3. A similar lack of OAT reactivity has been observed with the only other thiolate-ligated nonheme Fe^{IV}(O) complex.[38]

CONCLUSIONS

The thiolate-ligated nonheme iron complex $Fe^{II}(Me_3TACN)$-(S_2SiMe_2) (**1**) reacts with O_2 to generate a peroxo(diiron) species **2**. Complex **2** represents a rare example of a thiolate-ligated Fe/O_2 adduct, an unsupported nonheme diiron peroxo species, which was characterized by UV–vis, Mössbauer, RR, and X-ray absorption spectroscopies. The O–O bond of **2** can be cleaved to produce an $Fe^{IV}(O)$ species either photochemically or thermally. The resulting $Fe^{IV}(O)$ is capable of performing H atom abstraction with O–H bonds to produce an $Fe^{III}(OH)$ species, which could be independently synthesized via outer-sphere oxidation and addition of hydroxide (Scheme 5). Complex **3** is a thiolate-ligated $Fe^{IV}(O)$ species that is inert toward OAT to either the internal sulfur ligands or the exogenous O atom acceptors, yet readily abstracts H atoms from phenol substrates.

$Fe^{II}(Me_3TACN)(S_2SiMe_2)$ can also be compared to the Co analogue, $Co^{II}(Me_3TACN)(S_2SiMe_2)$,[39] which reacts with O_2 irreversibly to generate a mononuclear Co(superoxo) species. The differences in reactivity between the Co and Fe analogues may arise from reversibility of the formed M–O bond. A pair of Fe/Co superoxo complexes, $M(O_2)$(BDPP) (M = Fe, Co), was shown to exhibit marked differences in the reversibility of binding O_2, with Fe being able to release O_2 at −80 °C upon N_2 purging, whereas the analogous Co complex does not release O_2 below −90 °C.[35,86] We hypothesize that complex **2** is formed via the intermediacy of an Fe–superoxo intermediate that is in equilibrium with **1** and can readily release O_2 to capture another equivalent of Fe–superoxo, ultimately forming the Fe_2O_2 species **2**.

$Fe^{II}(Me_3TACN)(S_2SiMe_2)$ serves as a platform to activate O_2 to generate a series of Fe/oxygen intermediates (Fe(peroxo), Fe(oxo), and Fe(hydroxo) species), which could be trapped at low temperature and spectroscopically characterized (Scheme 5 and Table 4). This sequence of reactive species has been proposed in the activation of O_2 by iron and manganese complexes.[1,30,87–90] A crystallographically characterized thiolate-ligated Mn^{III}–O–O–Mn^{III} complex has been demonstrated to decay to an oxo-bridged Mn^{III}–O–Mn^{III}; however, no $Mn^{IV}(O)$ species was identified.[70] In addition, a similar thiolate-ligated Fe complex was shown to react with O_2 to form an $Fe^{III}_2(\mu\text{-O})$ complex. No intermediates were reported in the latter reaction, but a mechanism implicating formation of a peroxo-bridged dimer and O–O bond cleavage was suggested.[30] The silanedithiolato iron complex described here contains a ligand environment that allows for the generation and comparison of three O_2-derived species and provides direct evidence for O–O bond cleavage in a (peroxo)diiron complex to produce an $Fe^{IV}(O)$ complex. A major finding of this study is that mechanisms invoking O–O bond homolysis to generate high-valent metal–oxo complexes are feasible for O_2 activation by nonheme iron centers. This work also shows that metal-bound, reactive oxygen species can be supported by thiolate ligation, and establishes the viability of forming these Fe/O_2 intermediates in the presence of sulfur ligands without leading to immediate sulfur oxidation. These findings help to support similar proposed O_2 activation pathways in thiolate-ligated nonheme iron enzymes, demonstrating that the multistep binding and activation of O_2 at nonheme iron can take place prior to sulfur oxidation.

EXPERIMENTAL SECTION

Materials.

All syntheses and manipulations were conducted in an N_2-filled drybox (Vacuum Atmospheres, $O_2 < 0.2$ ppm, $H_2O < 0.5$ ppm) or using standard Schlenk techniques under an atmosphere of Ar unless otherwise noted. Me_3TACN was purchased from Matrix Scientific, degassed by three freeze–pump–thaw cycles, and stored over 3 Å molecular sieves. Hexamethylcyclotrisilathiane ($(Me_2SiS)_3$) was prepared according to a published procedure.[40] $Fe(OAc)_2$ was synthesized according to a published procedure.[91] $FcBAr^F{}_4$ and $^{Me2}FcBAr^F{}_4$ were prepared according to modified reported procedures[92] using $KBAr^F{}_4$ purchased from Boulder Scientific Co. (Mead, CO). Isotopically enriched ^{57}Fe metal (95.5%) was purchased from Cambridge Isotope Laboratories (Andover, MA). Isotopically enriched $57Fe(OAc)_2$ was synthesized according to a published procedure using ^{57}Fe powder.[93] $^{18}O_2$ (98 atom %) was purchased from ICON Isotopes (Summit, NJ). 4-OMe-TEMPOH was synthesized according to a published procedure.[94] 4-OMe-dtbp was purified by crystallization from hot ethanol and dried over P_2O_5 prior to use. All other reagents were purchased from commercial vendors and used without further purification. Methanol was distilled from CaH_2. Tetrahydrofuran, pentane, hexane, and 2-MeTHF were dried over Na/benzophenone and subsequently distilled. Diethyl ether was obtained from a PureSolv solvent purification system (SPS). All solvents were degassed by a minimum of three freeze–pump–thaw cycles and stored over freshly activated 3 Å molecular sieves in the drybox following distillation.

Instrumentation.

The ^1H spectra were measured on a Bruker 300 MHz or a Bruker 400 MHz spectrometer. Chemical shifts were referenced to reported solvent resonances.[95] UV–vis experiments were carried out on a Cary bio-50 or Cary 60 UV–vis spectrophotometer equipped with a Unisoku USP-203A cryostat using a 1 cm modified Schlenk cuvette. EPR measurements were performed on a Bruker X-band EPR in 5 mm quartz EPR tubes (Willmad). EPR spectral simulations were performed using Easy-Spin.[96] Cyclic voltammetry experiments were performed in a N_2 atmosphere drybox using a Princeton Applied Research Versastat II potentiostat and a three-electrode setup (1 mm platinum working electrode, Pt wire counter electrode, and a silverwire pseudoreference electrode) with electrodes purchased from BASi, Inc., and/or CH Instruments, Inc.

Computational Methods.

All geometry optimizations were performed in the ORCA-4.0.1.2 program package.[97] Initial geometries were obtained from the X-ray crystallographic model of **1** and altered as needed. Optimized geometries were calculated using the BP86 functional[98,99] or with B3LYP[100] for **3**, in combination with the D3 dispersion correction,[101] which gave satisfactory results in reproducing the experimentally derived bond metrics and vibrational frequencies. The basis set 6–311g* was used for all Fe, S, N, O, and Si atoms, and the 6–31g* basis set was used for all C and H atoms.[102–106] Solvent effects in these calculations were accounted for by using the conductor-like polarizable continuum model (CPCM), specifying the dielectric constant (ε) for THF in all cases except for **2**.[107] To reduce computational costs, the

Resolution of Identity (RI) approximations[108] in tandem with the def2/J auxiliary basis set[109] were employed. Because of SCF convergence difficulties in some cases, damping parameters were altered using the slowconv function in ORCA. Broken symmetry calculations were carried out,[110–112] and coupling contant J was calculated on the basis of the spin Hamiltonian $\hat{H} = -2J_{AB}\hat{S}_A \cdot \hat{S}_B$, where $J = (E_{HS} - E_{BS})/S_{max}^2$. E_{HS} and E_{BS} refer to the energies of the high and broken symmetry spin states.[110,111] Frequency calculations at the same level of theory confirmed that all optimizations had converged to true minima on the potential energy surface (i.e., no imaginary frequencies). The optimized structures were used for Mössbauer calculations. Mössbauer parameters were computed using the B3LYP[100] functional and a combination of CP(PPP)[113] for Fe and def2-TZVP[114,115] for all other atoms. The angular integration grid was set to Grid4 (NoFinalGrid), with increased radial accuracy for the Fe atom (IntAcc 7). To simulate solid state effects, a continuum solvation model was included (COSMO) with methanol designated as solvent, which has been shown to lead to accurate predictions of Mössbauer parameters.[43] The isomer shift was obtained from the electron density at the Fe nucleus, using a previously reported linear fit function, $\delta_{calc} = a(\rho(0) - C) + \beta$ where $a = -0.424$ mm s^{-1} au,[3] $\beta = 7.55$ mm s^{-1}, and $C = 11\,800$ au, [3] which was derived by plotting $\rho(0)$ versus the experimental isomer shift of a series of Fe complexes.[43] Single point calculations were carried out using the B3LYP[116] hybrid density functional. These calculations employed zeroth-order regular approximation (ZORA)[117–119] for relativistic effects. Single point calculations used the CP(PPP)[120,121] basis set on Fe and the ZORA-def2-TZVP(-f)[114,115,122] basis set on all other atoms.

Preparation of 2(^{57}Fe): Mössbauer Spectroscopy.

A solution of ^{57}Fe-enriched **1(^{57}Fe)** in 2-MeTHF was cooled to −135 °C. Excess O_2 was bubbled through the solution of **1(^{57}Fe)** in the dark, resulting in the formation of a dark green solution. The green solution was then poured into liquid nitrogen to form a frozen, dark green powder. The powder was pulverized with a spatula while being maintained under liquid nitrogen and then transferred into a Delrin Mössbauer cup fitted with a Delrin cap. The sample was stored under liquid nitrogen until it was loaded into the Mössbauer spectrometer.

Preparation of 2 and 3 for Resonance Raman Spectroscopy.

A stock solution of $Fe^{II}(Me_3TACN)(S_2SiMe_2)$ (**1**) was prepared in 2-MeTHF (4.5 mM). An aliquot of the stock solution of **1** was transferred to a 5 mm NMR tube and sealed with a septum in a drybox. The sealed NMR tube was removed from the drybox and cooled to −135 °C in a pentane/N_2(l) bath. Either $^{16}O_2$ (natural abundance, 2 mL) or $^{18}O_2$ (98%, 2 mL) was added to the solution of **1** in the dark, yielding a color change from colorless to dark green. The reaction was allowed to proceed with frequent manual mixing for 5 min, and then the reaction mixture containing **2** was slowly annealed in liquid nitrogen and stored at 77 K until needed. Samples of **3** were prepared by generating frozen samples of **2** and then exposing these samples to 619 nm LED light for 25 min, resulting in a color change from dark green to pale orange. Samples were stored at 77 K until needed. Resonance Raman (RR) spectra were obtained using a custom McPherson 2061/207 spectrograph (set at 0.67 m with variable gratings) equipped with a liquid nitrogen-cooled CCD detector (LN-1100PB, Princeton Instruments). After attempts with different laser excitations, the 407

and 351 nm lines from a Kr laser (Innova 300, Coherent) were selected for the RR characterizations of complexes **2** and **3**, respectively. Long-pass filters (RazorEdge, Semrock) were placed in front of the spectrograph entrance slit to attenuate the Rayleigh scattering. RR spectra were recorded using a 180° scattering geometry on samples maintained at 110 K inside a copper coldfinger and with continuous spinning. Frequencies were calibrated relative to aspirin and are accurate to ±1 cm^{-1}.

Preparation of 2: X-ray Absorption Spectroscopy.

A solution of ^{57}Fe-enriched **1(⁵⁷Fe)** (2 mL, 10.8 mM) in 2-MeTHF was cooled to −135 °C. Excess O_2 was bubbled through the solution of **1(⁵⁷Fe)** in the dark, resulting in the formation of a dark green solution. The green solution was then poured into liquid nitrogen to form a frozen, dark green powder. The powder was pulverized with a spatula while being maintained under liquid nitrogen and then transferred into a Delrin XAS cup with slits (1 × 4 mm). The slits were covered with Kapton tape (38 μm) to make X-ray transparent windows. All samples were ^{57}Fe-enriched for measurement by Mössbauer spectroscopy prior to XAS. Fe K-edge XAS data including extended X-ray absorption fine structure (EXAFS) data were obtained at the Stanford Synchrotron Lightsource Radiation (SSRL) at the 16-pole, 2 T wiggler beamline 9–3 under ring conditions of 3 GeV and 500 mA. A Si(220) double-crystal monochromator was used for energy selection. A Rh-coated mirror (set to an energy cutoff of 9 keV) was used for harmonic rejection, and the internal energy calibration was performed by assigning the first inflection point of an Fe foil spectrum to 7111.2 eV downstream of the sample. Data were collected in fluorescence mode (windowed onto Fe Kα_1) using a Canberra 30-element Ge moonlight solid-state detector perpendicular to the incident beam. Elastic scatter into the detector was attenuated using a Soller slit with an upstream Mn filter. During collection, samples were maintained at 10 K in an Oxford liquid He flow cryrostat, and 9 scans were obtained for each sample. Multiple spots were collected per sample, although there was no evidence of photodamage. The scans were averaged and processed using the SIXPACK software package.[123] A smooth pre-edge background was removed from each averaged spectrum by fitting a second-order polynomial to the pre-edge region and subtracting this polynomial from the entire spectrum. The postedge region was fit to a three-region cubic spline, flattened below 7130 eV, and then subtracted from the entire spectrum. Data were then normalized to a value of 1.0 at 7130 eV. EXAFS data were fit using the OPT module of the EXAFSPAK software package[124] with input scattering paths generated using FEFF7.[125,126]

Preparation of 3(⁵⁷Fe) for Mössbauer Spectroscopy.

Photolysis.—A solution of ^{57}Fe-enriched **1(⁵⁷Fe)** (1.5 mL, 6 mM) in 2-MeTHF was cooled to −135 °C. Excess O_2 was bubbled through the solution of **1(⁵⁷Fe)** in the dark, resulting in the formation of a dark green solution. The green solution was then poured into liquid nitrogen to form a dark green frozen powder. The powder was pulverized with a spatula while being maintained under liquid nitrogen. The pulverized powder was then covered with a glass Petri dish to filter out UV light and exposed to a 619 nm LED lamp for 30 min under liquid nitrogen, resulting in a color change from dark green to pale orange. The frozen powder was then transferred into a Delrin Mössbauer cup fitted with a Delrin

cap. The sample was stored under liquid nitrogen until it was loaded into the Mössbauer spectrometer.

Thermolysis.—A solution of ^{57}Fe-enriched **1(⁵⁷Fe)** (1.5 mL, 4.8 mM) in 2-MeTHF was cooled in a sealed vial at −105 °C. Excess O_2 was bubbled through the solution of **1(⁵⁷Fe)** in the dark, resulting in the formation of a dark green solution, which gradually turned pale orange over 15 min. The orange solution was then poured into liquid nitrogen to form a frozen, light orange powder. The powder was pulverized with a spatula while being maintained under liquid nitrogen and transferred into a Delrin Mössbauer cup fitted with a Delrin cap. The sample was stored under liquid nitrogen until it was loaded into the Mössbauer spectrometer.

Quantitation of 4 and Phenoxyl Radical by EPR Spectroscopy.

A stock solution of **1** was prepared in 2-MeTHF (1.1 mM). An aliquot of the stock solution (450 μL) of **1** was transferred into a 5 mm EPR tube and sealed with a septum in a drybox. The tube was removed from the drybox and cooled to −135 °C. Excess O_2 was then bubbled directly through the solution of **1** resulting in a color change from colorless to dark green. The sample was then frozen at 77 K and irradiated with a 619 nm LED bulb for 10 min resulting in a color change from dark green to pale orange. The solution was then warmed to −130 °C, and an aliquot of 4-OMe-dtbp (50 μL, 28 equiv in 2-MeTHF) was added. Manual mixing of the sample for 1 min resulted in a color change to dark orange red, and the sample was then slowly annealed in liquid nitrogen and stored at 77 K until needed.

Supplementary Material

Refer to Web version on PubMed Central for supplementary material.

ACKNOWLEDGMENTS

The NIH (GM119374 to D.P.G. and R35GM124908 to K.M.L.) is gratefully acknowledged for financial support. This work was also supported by an A. P. Sloan Research Fellowship to K.M.L. Computer time was provided by the Maryland Advanced Research Computing Center (MARCC). XAS data were obtained at SSRL, which is supported by the U.S. Department of Energy, Office of Science, Office of Basic Energy Sciences under contract no. DE-AC02-76SF00515. The SSRL Structural Molecular Biology Program is supported by the Department of Energy's Office of Biological and Environmental Research, and by NIH/NIGMS (including P41GM103393). We thank Prof. Guy N. L. Jameson (University of Melbourne) for helpful discussions.

REFERENCES

(1). Sahu S; Goldberg DP Activation of Dioxygen by Iron and Manganese Complexes: A Heme and Nonheme Perspective. J. Am. Chem. Soc 2016, 138, 11410–11428. [PubMed: 27576170]

(2). Hong S; Lee Y-M; Ray K; Nam W Dioxygen activation chemistry by synthetic mononuclear nonheme iron, copper and chromium complexes. Coord. Chem. Rev 2017, 334, 25–42.

(3). Que L Jr; Tolman WB Biologically inspired oxidation catalysis. Nature 2008, 455, 333–340. [PubMed: 18800132]

(4). Trammell R; Rajabimoghadam K; Garcia-Bosch I Copper-Promoted Functionalization of Organic Molecules: from Biologically Relevant Cu/O_2 Model Systems to Organometallic Transformations. Chem. Rev 2019, 119, 2954–3031. [PubMed: 30698952]

(5). Costas M Selective C–H oxidation catalyzed by metalloporphyrins. Coord. Chem. Rev 2011, 255, 2912–2932.

(6). Berkessel A Diversity-Based Approaches to Selective Biomimetic Oxidation Catalysis Advances in Inorganic Chemistry; Academic Press: New York, 2006; Vol. 58, pp 1–28.

(7). Costas M; Mehn MP; Jensen MP; Que L Jr. Dioxygen Activation at Mononuclear Nonheme Iron Active Sites: Enzymes, Models, and Intermediates. Chem. Rev 2004, 104, 939–986. [PubMed: 14871146]

(8). Balch AL; Chan Y-W; Cheng R-J; La Mar GN; Latos-Grazynski L; Renner MW Oxygenation Patterns for Iron(II) Porphyrins. Peroxo and Ferryl ($Fe^{IV}O$) Intermediates Detected by ^1H Nuclear Magnetic Resonance Spectroscopy during the Oxygenation of (Tetramesitylporphyrin)iron(II). J. Am. Chem. Soc 1984, 106, 7779–7785.

(9). Latos-Grazynski L; Cheng R-J; La Mar GN; Balch AL Oxygenation patterns for Substituted *meso*-Tetraphenylporphyrin Complexes of Iron(II). Spectroscopic Detection of Dioxygen Complexes in the Absence of Amines. J. Am. Chem. Soc 1982, 104, 5992–6000.

(10). Chin D-H; Balch AL; La Mar GN Formation of Porphyrin Ferryl (FeO^{2+}) Complexes through the Addition of Nitrogen Bases to Peroxo-Bridged Iron(III) Porphyrins. J. Am. Chem. Soc 1980, 102, 1446–1448.

(11). Chin D-H; La Mar GN; Balch AL Mechanism of autoxidation of iron(II) porphyrins. Detection of a peroxo-bridged iron(III) porphyrin dimer and the mechanism of its thermal decomposition to the oxo-bridged iron(III) porphyrin dimer. J. Am. Chem. Soc 1980, 102, 4344–4350.

(12). Chin D-H; Del Gaudio J; La Mar GN; Balch AL Detection and Characterization of the Long-Postulated Fe-OO-Fe Intermediate in the Autoxidation of Ferrous Porphyrins. J. Am. Chem. Soc 1977, 99, 5486–5488. [PubMed: 886109]

(13). Orville AM; Chen VJ; Kriauciunas A; Harpel MR; Fox BG; Münck E; Lipscomb JD Thiolate Ligation of the Active Site Fe^{2+} of Isopenicillin N Synthase Derives from Substrate Rather Than Endogenous Cysteine: Spectroscopic Studies of Site-Specific Cys→Ser Mutated Enzymes. Biochemistry 1992, 31, 4602–4612. [PubMed: 1316153]

(14). Roach PL; Clifton IJ; Hensgens CMH; Shibata N; Schofield CJ; Hajdu J; Baldwin JE Structure of isopenicillin *N* synthase complexed with substrate and the mechanism of penicillin formation. Nature 1997, 387, 827–830. [PubMed: 9194566]

(15). Ye S; Wu X; Wei L; Tang D; Sun P; Bartlam M; Rao Z An Insight into the Mechanism of Human Cysteine Dioxygenase: KEY ROLES OF THE THIOETHER-BONDED TYROSINECYSTEINE COFACTOR. J. Biol. Chem 2007, 282, 3391–3402. [PubMed: 17135237]

(16). Aloi S; Davies CG; Karplus PA; Wilbanks SM; Jameson GNL Substrate Specificity in Thiol Dioxygenases. Biochemistry 2019, 58, 2398–2407. [PubMed: 31045343]

(17). Goncharenko KV; Vit A; Blankenfeldt W; Seebeck FP Structure of the Sulfoxide Synthase EgtB from the Ergothioneine Biosynthetic Pathway. Angew. Chem., Int. Ed 2015, 54, 2821–2824.

(18). Naowarojna N; Cheng R; Chen L; Quill M; Xu M; Zhao C; Liu P Mini-Review: Ergothioneine and Ovothiol Biosyntheses, an Unprecedented Trans-Sulfur Strategy in Natural Product Biosynthesis. Biochemistry 2018, 57, 3309–3325. [PubMed: 29589901]

(19). Tamanaha E; Zhang B; Guo Y; Chang W.-c.; Barr EW; Xing G; Clair J St.; Ye S; Neese F; Bollinger JM Jr.; Krebs C Spectroscopic Evidence for the Two C–H-Cleaving Intermediates of *Aspergillus nidulans* Isopenicillin *N* Synthase. J. Am. Chem. Soc 2016, 138, 8862–8874. [PubMed: 27193226]

(20). Tchesnokov EP; Faponle AS; Davies CG; Quesne MG; Turner R; Fellner M; Souness RJ; Wilbanks SM; de Visser SP; Jameson GNL An iron-oxygen intermediate formed during the catalytic cycle of cysteine dioxygenase. Chem. Commun 2016, 52, 8814–8817.

(21). Stampfli AR; Goncharenko KV; Meury M; Dubey BN; Schirmer T; Seebeck FP An Alternative Active Site Architecture for O_2 Activation in the Ergothioneine Biosynthetic EgtB from *Chloracidobacterium thermophilum*. J. Am. Chem. Soc 2019, 141, 5275–5285. [PubMed: 30883103]

(22). Song H; Her AS; Raso F; Zhen Z; Huo Y; Liu P Cysteine Oxidation Reactions Catalyzed by a Mononuclear Non-heme Iron Enzyme (OvoA) in Ovothiol Biosynthesis. Org. Lett 2014, 16, 2122–2125. [PubMed: 24684381]

(23). Jiang Y; Widger LR; Kasper GD; Siegler MA; Goldberg DP Iron(II)-Thiolate *S*-Oxygenation by O_2: Synthetic Models of Cysteine Dioxygenase. J. Am. Chem. Soc 2010, 132, 12214–12215. [PubMed: 20712312]

(24). Badiei YM; Siegler MA; Goldberg DP O_2 Activation by Bis(imino)pyridine Iron(II)-Thiolate Complexes. J. Am. Chem. Soc 2011, 133, 1274–1277. [PubMed: 21207980]

(25). McQuilken AC; Jiang Y; Siegler MA; Goldberg DP Addition of Dioxygen to an N4S(thiolate) Iron(II) Cysteine Dioxygenase Model Gives a Structurally Characterized Sulfinato–Iron(II) Complex. J. Am. Chem. Soc 2012, 134, 8758–8761. [PubMed: 22578255]

(26). Widger LR; Siegler MA; Goldberg DP Sulfide oxidation by O_2: Synthesis, structure and reactivity of novel sulfide-incorporated Fe(II) bis(imino)pyridine complexes. Polyhedron 2013, 58, 179–189. [PubMed: 23878411]

(27). Gordon JB; McGale JP; Prendergast JR; Shirani-Sarmazeh Z; Siegler MA; Jameson GNL; Goldberg DP Structures, Spectroscopic Properties, and Dioxygen Reactivity of 5- and 6-Coordinate Nonheme Iron(II) Complexes: A Combined Enzyme/Model Study of Thiol Dioxygenases. J. Am. Chem. Soc 2018, 140, 14807–14822. [PubMed: 30346746]

(28). Musie G; Lai C-H; Reibenspies JH; Sumner LW; Darensbourg MY Pentacoordinate (μ-Oxo)diiron(III) Thiolate Complexes and Dimeric Iron(II) Precursors. Inorg. Chem 1998, 37, 4086–4093. [PubMed: 11670528]

(29). Blakely MN; Dedushko MA; Poon PCY; Villar-Acevedo G; Kovacs JA Formation of a Reactive, Alkyl Thiolate-Ligated Fe^{III}-Superoxo Intermediate Derived from Dioxygen. J. Am. Chem. Soc 2019, 141, 1867–1870. [PubMed: 30661357]

(30). Theisen RM; Shearer J; Kaminsky W; Kovacs JA Steric and Electronic Control over the Reactivity of a Thiolate-Ligated Fe(II) Complex with Dioxygen and Superoxide: Reversible μ-Oxo Dimer Formation. Inorg. Chem 2004, 43, 7682–7690. [PubMed: 15554633]

(31). Sallmann M; Braun B; Limberg C Dioxygenation of cysteamine to hypotaurine at a tris(pyrazolyl)borate iron(ii) unit -cysteamine dioxygenase mimicking? Chem. Commun 2015, 51, 6785–6787.

(32). Sallmann M; Siewert I; Fohlmeister L; Limberg C; Knispel C A Trispyrazolylborato Iron Cysteinato Complex as a Functional Model for the Cysteine Dioxygenase. Angew. Chem., Int. Ed 2012, 51, 2234–2237.

(33). Fischer AA; Lindeman SV; Fiedler AT A synthetic model of the nonheme iron–superoxo intermediate of cysteine dioxygenase. Chem. Commun 2018, 54, 11344–11347.

(34). Fischer AA; Stracey N; Lindeman SV; Brunold TC; Fiedler AT Synthesis, X-ray Structures, Electronic Properties, and O_2/NO Reactivities of Thiol Dioxygenase Active-Site Models. Inorg. Chem 2016, 55, 11839–11853. [PubMed: 27801576]

(35). Chiang C-W; Kleespies ST; Stout HD; Meier KK; Li P-Y; Bominaar EL; Que L Jr.; Münck E; Lee W-Z Characterization of a Paramagnetic Mononuclear Nonheme Iron-Superoxo Complex. J. Am. Chem. Soc 2014, 136, 10846–10849. [PubMed: 25036460]

(36). Oddon F; Chiba Y; Nakazawa J; Ohta T; Ogura T; Hikichi S Characterization of Mononuclear Non-heme Iron(III)-Superoxo Complex with a Five-Azole Ligand Set. Angew. Chem., Int. Ed 2015, 54, 7336–7339.

(37). Jasniewski AJ; Que L Jr. Dioxygen Activation by Nonheme Diiron Enzymes: Diverse Dioxygen Adducts, High-Valent Intermediates, and Related Model Complexes. Chem. Rev 2018, 118, 2554–2592. [PubMed: 29400961]

(38). Bukowski MR; Koehntop KD; Stubna A; Bominaar EL; Halfen JA; Münck E; Nam W; Que L Jr. A thiolate-ligated nonheme oxoiron(IV) complex relevant to cytochrome P450. Science 2005, 310, 1000–1002. [PubMed: 16254150]

(39). Gordon JB; Vilbert AC; Siegler MA; Lancaster KM; Moënne-Loccoz P; Goldberg DP A Nonheme Thiolate-Ligated Cobalt Superoxo Complex: Synthesis and Spectroscopic Characterization, Computational Studies, and Hydrogen Atom Abstraction Reactivity. J. Am. Chem. Soc 2019, 141, 3641–3653. [PubMed: 30776222]

(40). Komuro T; Matsuo T; Kawaguchi H; Tatsumi K Coordination Chemistry of Silanedithiolato Ligands Derived from Cyclotrisilathiane: Synthesis and Structures of Complexes of Iron(II),

Cobalt(II), Palladium(II), Copper(I), and Silver(I). Inorg. Chem 2003, 42, 5340–5347. [PubMed: 12924906]

(41). Lacy DC Applications of the Marcus cross relation to inner sphere reduction of O2: implications in small-molecule activation. Inorg. Chem. Front 2019, 6, 2396.

(42). Hagen WR Biomolecular EPR Spectroscopy; CRC Press: Boca Raton, FL, 2009.

(43). Pápai M; Vankó G On Predicting Mössbauer Parameters of Iron-Containing Molecules with Density-Functional Theory. J. Chem. Theory Comput 2013, 9, 5004–5020. [PubMed: 25821417]

(44). Bochevarov AD; Friesner RA; Lippard SJ Prediction of ^{57}Fe Mössbauer Parameters by Density Functional Theory: A Benchmark Study. J. Chem. Theory Comput 2010, 6, 3735–3749. [PubMed: 21258606]

(45). Gütlich P; Bill E; Trautwein A Mössbauer Spectroscopy and Transition Metal Chemistry: Fundamentals and Applications; Springer-Verlag: Berlin, 2011.

(46). Dong Y; Zang Y; Shu L; Wilkinson EC; Que L Jr.; Kauffmann K; Münck E Models for Nonheme Diiron Enzymes. Assembly of a High-Valent $Fe_2(\mu\text{-}O)_2$ Diamond Core from Its Peroxo Precursor. J. Am. Chem. Soc 1997, 119, 12683–12684.

(47). Dong Y; Ménage S; Brennan BA; Elgren TE; Jang HG; Pearce LL; Que L Jr. Dioxygen Binding to Diferrous Centers. Models for Diiron-Oxo Proteins. J. Am. Chem. Soc 1993, 115, 1851–1859.

(48). Kim K; Lippard SJ Structure and Mössbauer Spectrum of a (μ–1,2-Peroxo)bis(μ-carboxylato)diiron(III) Model for the Peroxo Intermediate in the Methane Monooxygenase Hydroxylase Reaction Cycle. J. Am. Chem. Soc 1996, 118, 4914–4915.

(49). Brunold TC; Tamura N; Kitajima N; Moro-Oka Y; Solomon EI Spectroscopic Study of $[Fe_2(O_2)(OBz)_2\{HB(pz')_3\}]_2$: Nature of the μ–1,2 Peroxide-Fe(III) Bond and Its Possible Relevance to O_2 Activation by Non-Heme Iron Enzymes. J. Am. Chem. Soc 1998, 120, 5674–5690.

(50). Nakamoto K Infrared and Raman Spectra of Inorganic and Coordination Compounds, Theory and Applications in Inorganic Chemistry; Wiley: New York, 1997.

(51). Ookubo T; Sugimoto H; Nagayama T; Masuda H; Sato T; Tanaka K; Maeda Y; Okawa H; Hayashi Y; Uehara A; Suzuki M *cis*-μ–1,2-Peroxo Diiron Complex: Structure and Reversible Oxygenation. J. Am. Chem. Soc 1996, 118, 701–702.

(52). Hagadorn JR; Que L Jr.; Tolman WB A Bulky Benzoate Ligand for Modeling the Carboxylate-Rich Active Sites of Non-Heme Diiron Enzymes. J. Am. Chem. Soc 1998, 120, 13531–13532. [PubMed: 28926239]

(53). Friedle S; Kodanko JJ; Morys AJ; Hayashi T; Moënne-Loccoz P; Lippard SJ Modeling the Syn Disposition of Nitrogen Donors in Non-Heme Diiron Enzymes. Synthesis, Characterization, and Hydrogen Peroxide Reactivity of Diiron(III) Complexes with the Syn *N*-Donor Ligand H_2BPG_2DEV. J. Am. Chem. Soc 2009, 131, 14508–14520. [PubMed: 19757795]

(54). Kodera M; Tsuji T; Yasunaga T; Kawahara Y; Hirano T; Hitomi Y; Nomura T; Ogura T; Kobayashi Y; Sajith PK; Shiota Y; Yoshizawa K Roles of carboxylate donors in O–O bond scission of peroxodi-iron(iii) to high-spin oxodi-iron(iv) with a new carboxylate-containing dinucleating ligand. Chem. Sci 2014, 5, 2282–2292.

(55). Sekino M; Furutachi H; Tasaki K; Ishikawa T; Mori S; Fujinami S; Akine S; Sakata Y; Nomura T; Ogura T; Kitagawa T; Suzuki M New mechanistic insight into intramolecular arene hydroxylation initiated by (μ–1,2-peroxo)diiron(iii) complexes with dinucleating ligands. Dalton Trans 2016, 45, 469–473. [PubMed: 26646073]

(56). Long TV II; Loehr TM; Allkins JR; Lovenberg W Determination of iron coordination in nonheme iron proteins using laser-Raman spectroscopy. II. Clostridium pasteurianum rubredoxin in aqueous solution. J. Am. Chem. Soc 1971, 93, 1809–1811. [PubMed: 5550254]

(57). Champion PM; Stallard BR; Wagner GC; Gunsalus IC Resonance Raman detection of an iron-sulfur bond in cytochrome $P450_{cam}$. J. Am. Chem. Soc 1982, 104, 5469–5472.

(58). Xiao Z; Lavery MJ; Ayhan M; Scrofani SDB; Wilce MCJ; Guss JM; Tregloan PA; George GN; Wedd AG The Rubredoxin from *Clostridium pasteurianum*: Mutation of the Iron Cysteinyl Ligands to Serine. Crystal and Molecular Structures of Oxidized and Dithionite-Treated Forms of the Cys42Ser Mutant. J. Am. Chem. Soc 1998, 120, 4135–4150.

(59). Tshuva EY; Lippard SJ Synthetic Models for Non-Heme Carboxylate-Bridged Diiron Metalloproteins: Strategies and Tactics. Chem. Rev 2004, 104, 987–1012. [PubMed: 14871147]

(60). Lindblom LA; Schaefer WP; Marsh RE The Crystal and Molecular Structure of μ-peroxo-bis-[3,3′-diimino-di-n-propylamine-bis-salicylaldehyde cobalt(III)]. $C_6H_5CH_3$. Acta Crystallogr., Sect. B: Struct. Crystallogr. Cryst. Chem 1971, 27, 1461–1467.

(61). Gainsford GJ; Jackson WG; Sargeson AM Novel Synthesis and Structure of a Bridging Peroxo Pentaaminecobalt(III) Dimer. Aust. J. Chem 1986, 39, 1331–1336.

(62). Zehnder M; Thewalt U Mehrkernige Kobaltkomplexe. IV. Darstellung und Struktur von [(papd)Co(O_2)Co(papd)](S_2O_6)-(NO_3)2 2 4 H_2O). Z. Anorg. Allg. Chem 1980, 461, 53–60.

(63). Dedushko MA; Schweitzer D; Blakely MN; Swartz RD; Kaminsky W; Kovacs JA Geometric and electronic structure of a crystallographically characterized thiolate-ligated binuclear peroxo-bridged cobalt(III) complex. JBIC, J. Biol. Inorg. Chem 2019, 24, 919. [PubMed: 31342141]

(64). Riggs-Gelasco PJ; Stemmler TL; Penner-Hahn JE XAFS of dinuclear metal sites in proteins and model compounds. Coord. Chem. Rev 1995, 144, 245–286.

(65). Cranswick MA; Meier KK; Shan X; Stubna A; Kaizer J; Mehn MP; Münck E; Que L Jr. Protonation of a Peroxodiiron-(III) Complex and Conversion to a Diiron(III/IV) Intermediate: Implications for Proton-Assisted O–O Bond Cleavage in Nonheme Diiron Enzymes. Inorg. Chem 2012, 51, 10417–10426. [PubMed: 22971084]

(66). Frisch JR; Vu VV; Martinho M; Münck E; Que L Jr. Characterization of Two Distinct Adducts in the Reaction of a Nonheme Diiron(II) Complex with O_2. Inorg. Chem 2009, 48, 8325–8336. [PubMed: 19610611]

(67). Rodima T; Kaljurand I; Pihl A; Mäemets V; Leito I; Koppel IA Acid-Base Equilibria in Nonpolar Media. 2. Self-Consistent Basicity Scale in THF Solution Ranging from 2-Methoxypyridine to EtP1(pyrr) Phosphazene. J. Org. Chem 2002, 67, 1873–1881. [PubMed: 11895405]

(68). Baga AN; Johnson GRA; Nazhat NB; Saadalla-Nazhat RA A simple spectrophotometric determination of hydrogen peroxide at low concentrations in aqueous solution. Anal. Chim. Acta 1988, 204, 349–353.

(69). Kundu S; Matito E; Walleck S; Pfaff FF; Heims F; Rábay B; Luis JM; Company A; Braun B; Glaser T; Ray K O—O Bond Formation Mediated by a Hexanuclear Iron Complex Supported on a Stannoxane Core. Chem. - Eur. J 2012, 18, 2787–2791. [PubMed: 22262528]

(70). Coggins MK; Sun X; Kwak Y; Solomon EI; Rybak-Akimova E; Kovacs JA Characterization of Metastable Intermediates Formed in the Reaction between a Mn(II) Complex and Dioxygen, Including a Crystallographic Structure of a Binuclear Mn(III)–Peroxo Species. J. Am. Chem. Soc 2013, 135, 5631–5640. [PubMed: 23470101]

(71). Bailey WD; Dhar D; Cramblitt AC; Tolman WB Mechanistic Dichotomy in Proton-Coupled Electron-Transfer Reactions of Phenols with a Copper Superoxide Complex. J. Am. Chem. Soc 2019, 141, 5470–5480. [PubMed: 30907590]

(72). McDonald AR; Que L Jr. High-valent nonheme iron-oxo complexes: Synthesis, structure, and spectroscopy. Coord. Chem. Rev 2013, 257, 414–428.

(73). Jackson TA; Rohde J-U; Seo MS; Sastri CV; DeHont R; Stubna A; Ohta T; Kitagawa T; Münck E; Nam W; Que L Jr. Axial Ligand Effects on the Geometric and Electronic Structures of Nonheme Oxoiron(IV) Complexes. J. Am. Chem. Soc 2008, 130, 12394–12407. [PubMed: 18712873]

(74). Mizutani Y; Hashimoto S; Tatsuno Y; Kitagawa T Resonance Raman Pursuit of the Change from Fe^{II}-O_2 to Fe^{III}-OH via Fe^{IV}=O in the Autoxidation of Ferrous Iron-Porphyrin. J. Am. Chem. Soc 1990, 112, 6809–6814.

(75). Kitagawa T; Mizutani Y Resonance Raman spectra of highly oxidized metalloporphyrins and heme proteins. Coord. Chem. Rev 1994, 135–136, 685–735.

(76). Andris E; Navrátil R; Jašík J; Puri M; Costas M; Que L; Roithová J Trapping Iron(III)–Oxo Species at the Boundary of the “Oxo Wall”: Insights into the Nature of the Fe(III)–O Bond. J. Am. Chem. Soc 2018, 140, 14391–14400. [PubMed: 30336001]

(77). Behan RK; Green MT On the status of ferryl protonation. J. Inorg. Biochem 2006, 100, 448–459. [PubMed: 16500711]

(78). Spaeth AD; Gagnon NL; Dhar D; Yee GM; Tolman WB Determination of the Cu(III)–OH Bond Distance by Resonance Raman Spectroscopy Using a Normalized Version of Badger’s Rule. J. Am. Chem. Soc 2017, 139, 4477–4485. [PubMed: 28319386]

(79). Chanda A; Shan X; Chakrabarti M; Ellis WC; Popescu DL; Tiago de Oliveira F; Wang D; Que L; Collins TJ; Münck E; Bominaar EL (TAML)FeIV=O Complex in Aqueous Solution: Synthesis and Spectroscopic and Computational Characterization. Inorg. Chem 2008, 47, 3669–3678. [PubMed: 18380453]

(80). Green MT; Dawson JH; Gray HB Oxoiron(IV) in Chloroperoxidase Compound II Is Basic: Implications for P450 Chemistry. Science 2004, 304, 1653–1656. [PubMed: 15192224]

(81). Wang B; Lee Y-M; Tcho W-Y; Tussupbayev S; Kim S-T; Kim Y; Seo MS; Cho K-B; Dede Y; Keegan BC; Ogura T; Kim SH; Ohta T; Baik M-H; Ray K; Shearer J; Nam W Synthesis and reactivity of a mononuclear non-haem cobalt(IV)-oxo complex. Nat. Commun 2017, 8, 14839. [PubMed: 28337985]

(82). Ching W-M; Zhou A; Klein JEMN; Fan R; Knizia G; Cramer CJ; Guo Y; Que L Characterization of the Fleeting Hydroxoiron(III) Complex of the Pentadentate TMC-py Ligand. Inorg. Chem 2017, 56, 11129–11140. [PubMed: 28858496]

(83). Mukherjee J; Lucas RL; Zart MK; Powell DR; Day VW; Borovik AS Synthesis, Structure, and Physical Properties for a Series of Monomeric Iron(III) Hydroxo Complexes with Varying Hydrogen-Bond Networks. Inorg. Chem 2008, 47, 5780–5786. [PubMed: 18498155]

(84). Yadav V; Gordon JB; Siegler MA; Goldberg DP Dioxygen-Derived Nonheme Mononuclear FeIII(OH) Complex and Its Reactivity with Carbon Radicals. J. Am. Chem. Soc 2019, 141, 10148–10153. [PubMed: 31244183]

(85). Mayer JM Understanding Hydrogen Atom Transfer: From Bond Strengths to Marcus Theory. Acc. Chem. Res 2011, 44, 36–46. [PubMed: 20977224]

(86). Wang C-C; Chang H-C; Lai Y-C; Fang H; Li C-C; Hsu H-K; Li Z-Y; Lin T-S; Kuo T-S; Neese F; Ye S; Chiang Y-W; Tsai M-L; Liaw W-F; Lee W-Z A Structurally Characterized Nonheme Cobalt–Hydroperoxo Complex Derived from Its Superoxo Intermediate via Hydrogen Atom Abstraction. J. Am. Chem. Soc 2016, 138, 14186–14189. [PubMed: 27726348]

(87). Kim SO; Sastri CV; Seo MS; Kim J; Nam W Dioxygen Activation and Catalytic Aerobic Oxidation by a Mononuclear Nonheme Iron(II) Complex. J. Am. Chem. Soc 2005, 127, 4178–4179. [PubMed: 15783193]

(88). Wijeratne GB; Corzine B; Day VW; Jackson TA Saturation Kinetics in Phenolic O–H Bond Oxidation by a Mononuclear Mn(III)–OH Complex Derived from Dioxygen. Inorg. Chem 2014, 53, 7622–7634. [PubMed: 25010596]

(89). MacBeth CE; Golombek AP; Young VG Jr.; Yang C; Kuczera K; Hendrich MP; Borovik AS O_2 Activation by Nonheme Iron Complexes: A Monomeric Fe(III)-Oxo Complex Derived From O_2. Science 2000, 289, 938–941. [PubMed: 10937994]

(90). Parham JD; Wijeratne GB; Mayfield JR; Jackson TA Steric control of dioxygen activation pathways for MnII complexes supported by pentadentate, amide-containing ligands. Dalton Trans 2019, 48, 13034. [PubMed: 31406966]

(91). Catterick J; Thornton P; Fitzsimmons BW Synthesis, magnetic properties, and Mössbauer spectra of polynuclear iron carboxylates. J. Chem. Soc., Dalton Trans 1977, 1420–1425.

(92). Chávez I; Alvarez-Carena A; Molins E; Roig A; Maniukiewicz W; Arancibia A; Arancibia V; Brand H; Manuel Manrßquez J Selective oxidants for organometallic compounds containing a stabilising anion of highly reactive cations: $(3,5\text{-}(CF3)_2C_6H_3)_4B^-)Cp_2Fe^+$ and $(3,5(CF_3)_2C_6H_3)_4B^-)Cp^*_2Fe^+$. J. Organomet. Chem 2000, 601, 126–132.

(93). Weber B; Betz R; Bauer W; Schlamp S Crystal Structure of Iron(II) Acetate. Z. Anorg. Allg. Chem 2011, 637, 102–107.

(94). Wu A; Mader EA; Datta A; Hrovat DA; Borden WT; Mayer JM Nitroxyl Radical Plus Hydroxylamine Pseudo Self-Exchange Reactions: Tunneling in Hydrogen Atom Transfer. J. Am. Chem. Soc 2009, 131, 11985–11997. [PubMed: 19618933]

(95). Fulmer GR; Miller AJM; Sherden NH; Gottlieb HE; Nudelman A; Stoltz BM; Bercaw JE; Goldberg KI NMR Chemical Shifts of Trace Impurities: Common Laboratory Solvents, Organics, and Gases in Deuterated Solvents Relevant to the Organometallic Chemist. Organometallics 2010, 29, 2176–2179.

(96). Stoll S; Schweiger A EasySpin, a comprehensive software package for spectral simulation and analysis in EPR. J. Magn. Reson 2006, 178, 42–55. [PubMed: 16188474]

(97). Neese F Software update: the ORCA program system, version 4.0. WIREs Comput. Mol. Sci 2018, 8, No. e1327.

(98). Perdew JP Density-functional approximation for the correlation energy of the inhomogeneous electron gas. Phys. Rev. B: Condens. Matter Mater. Phys 1986, 33, 8822–8824.

(99). Becke AD Completely numerical calculations on diatomic molecules in the local-density approximation. Phys. Rev. A: At., Mol., Opt. Phys 1986, 33, 2786–2788.

(100). Becke AD Density-functional thermochemistry. III. The role of exact exchange. J. Chem. Phys 1993, 98, 5648–5652.

(101). Grimme S; Antony J; Ehrlich S; Krieg H A consistent and accurate ab *initio* parametrization of density functional dispersion correction (DFT-D) for the 94 elements H-Pu. J. Chem. Phys 2010, 132, 154104. [PubMed: 20423165]

(102). Krishnan R; Binkley JS; Seeger R; Pople JA Self-consistent molecular orbital methods. XX. A basis set for correlated wave functions. J. Chem. Phys 1980, 72, 650–654.

(103). McLean AD; Chandler GS Contracted Gaussian basis sets for molecular calculations. I. Second row atoms, Z = 11–18. J. Chem. Phys 1980, 72, 5639–5648.

(104). Blaudeau J-P; McGrath MP; Curtiss LA; Radom L Extension of Gaussian-2 (G2) theory to molecules containing third-row atoms K and Ca. J. Chem. Phys 1997, 107, 5016–5021.

(105). Curtiss LA; McGrath MP; Blaudeau J-P; Davis NE; Binning RC Jr.; Radom L Extension of Gaussian-2 theory to molecules containing third-row atoms Ga–Kr. J. Chem. Phys 1995, 103, 6104–6113.

(106). Clark T; Chandrasekhar J; Spitznagel GW; Schleyer P v. R. Efficient diffuse function-augmented basis sets for anion calculations. III. The 3–21+G basis set for first-row elements, Li–F. J. Comput. Chem 1983, 4, 294–301.

(107). Marenich AV; Cramer CJ; Truhlar DG Universal solvation model based on solute electron density and on a continuum model of the solvent defined by the bulk dielectric constant and atomic surface tensions. J. Phys. Chem. B 2009, 113, 6378–6396. [PubMed: 19366259]

(108). Neese F; Wennmohs F; Hansen A; Becker U Efficient, approximate and parallel Hartree–Fock and hybrid DFT calculations. A 'chain-of-spheres' algorithm for the Hartree–Fock exchange. Chem. Phys 2009, 356, 98–109.

(109). Eichkorn K; Treutler O; Öhm H; Häser M; Ahlrichs R Auxiliary basis sets to approximate Coulomb potentials. Chem. Phys. Lett 1995, 240, 283–290.

(110). Noodleman L; Davidson ER Ligand spin polarization and antiferromagnetic coupling in transition metal dimers. Chem. Phys 1986, 109, 131–143.

(111). Noodleman L Valence bond description of antiferromagnetic coupling in transition metal dimers. J. Chem. Phys 1981, 74, 5737–5743.

(112). Ginsberg AP Magnetic Exchange in Transition Metal Complexes. 12. Calculation of Cluster Exchange Coupling Constants with the Xα-Scattered Wave Method. J. Am. Chem. Soc 1980, 102, 111–117.

(113). Römelt M; Ye S; Neese F Calibration of modern density functional theory methods for the prediction of ^{57}Fe Mossbauer isomer shifts: meta-GGA and double-hybrid functionals. Inorg. Chem 2009, 48, 784–785. [PubMed: 19102678]

(114). Weigend F; Ahlrichs R Balanced basis sets of split valence, triple zeta valence and quadruple zeta valence quality for H to Rn: Design and assessment of accuracy. Phys. Chem. Chem. Phys 2005, 7, 3297–3305. [PubMed: 16240044]

(115). Schäfer A; Horn H; Ahlrichs R Fully Optimized Contracted Gaussian-Basis Sets for Atoms Li to Kr. J. Chem. Phys 1992, 97, 2571–2577.

(116). Stephens PJ; Devlin FJ; Chabalowski CF; Frisch MJ *Ab Initio* Calculation of Vibrational Absorption and Circular Dichroism Spectra Using Density Functional Force Fields. J. Phys. Chem 1994, 98, 11623–11627.

(117). Lenthe E. v.; Baerends EJ; Snijders JG Relativistic regular two-component Hamiltonians. J. Chem. Phys 1993, 99, 4597–4610.

(118). Lenthe E. v.; Baerends EJ; Snijders JG Relativistic total energy using regular approximations. J. Chem. Phys 1994, 101, 9783–9792.

(119). Wüllen C v. Molecular density functional calculations in the regular relativistic approximation: Method, application to coinage metal diatomics, hydrides, fluorides and chlorides, and comparison with first-order relativistic calculations. J. Chem. Phys 1998, 109, 392–399.

(120). Neese F Prediction and interpretation of the ^{57}Fe isomer shift in Mössbauer spectra by density functional theory. Inorg. Chim. Acta 2002, 337, 181–192.

(121). Hedegård ED; Kongsted J; Sauer SPA Improving the calculation of electron paramagnetic resonance hyperfine coupling tensors for d-block metals. Phys. Chem. Chem. Phys 2012, 14, 10669–10676. [PubMed: 22785432]

(122). Schäfer A; Huber C; Ahlrichs R Fully optimized contracted Gaussian basis sets of triple zeta valence quality for atoms Li to Kr. J. Chem. Phys 1994, 100, 5829–5835.

(123). Webb SM SIXpack: a graphical user interface for XAS analysis using IFEFFIT. Phys. Scr 2005, 2005, 1011.

(124). George GN EXAFSPAK. Stanford Synchrotron Radiation Lightsource, S. L. A. C; Stanford University.

(125). Mustre de Leon J; Rehr JJ; Zabinsky SI; Albers RC *Ab initio* curved-wave x-ray-absorption fine structure. Phys. Rev. B: Condens. Matter Mater. Phys 1991, 44, 4146–4156.

(126). Rehr JJ; Mustre de Leon J; Zabinsky SI; Albers RC Theoretical x-ray absorption fine structure standards. J. Am. Chem. Soc 1991, 113, 5135–5140.

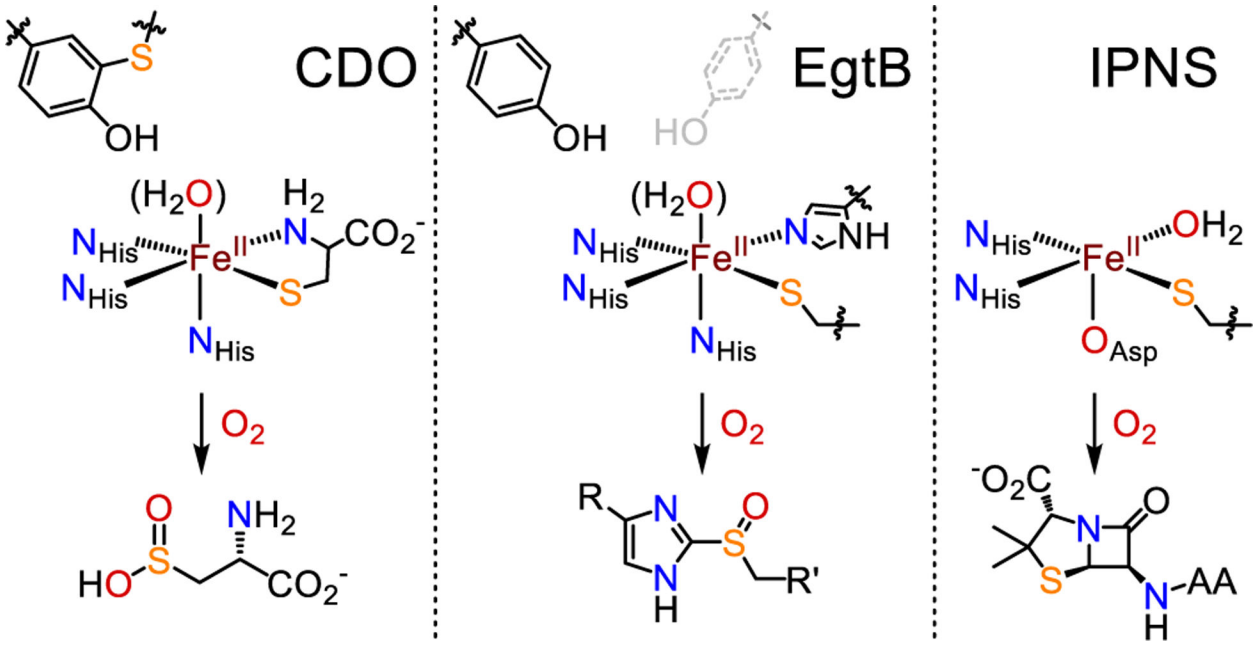

Figure 1.
Reactions of CDO, EgtB, and IPNS.

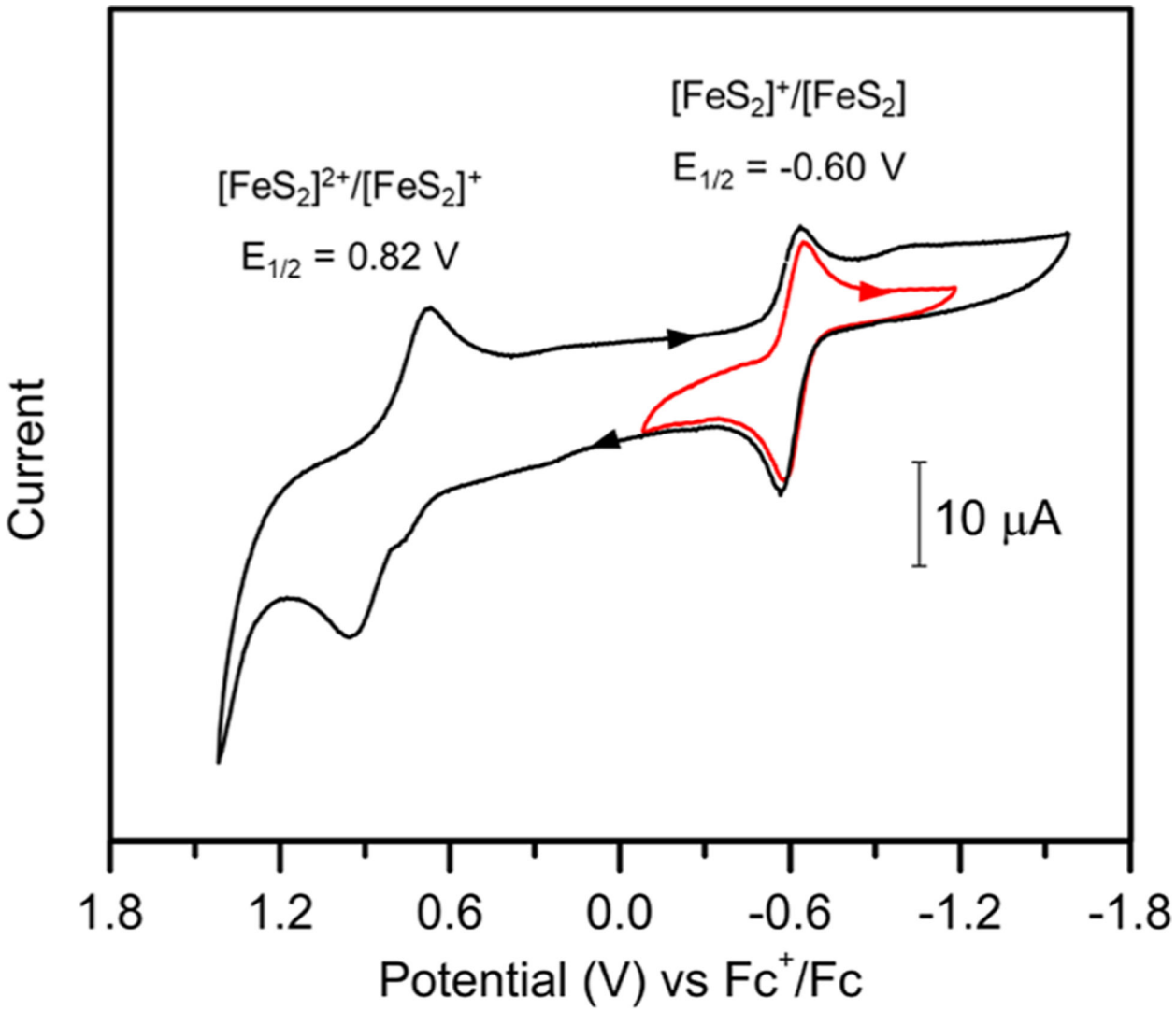

Figure 2.

Cyclic voltammogram of **1** (5 mM) in CH_3CN at 23 °C, with $^{n}Bu_4NPF_6$ (0.3 M) as supporting electrolyte. Working electrode, glassy carbon; reference electrode, Ag wire; counter electrode, Pt wire. Scan rate: 50 mV s^{-1}. Black line corresponds to full scan window from 1.4 to −1.6 V. Red line corresponds to isolated $[FeS^{2}]^{+}/[FeS_2]^{0}$ event from −0.1 to −1.2 V.

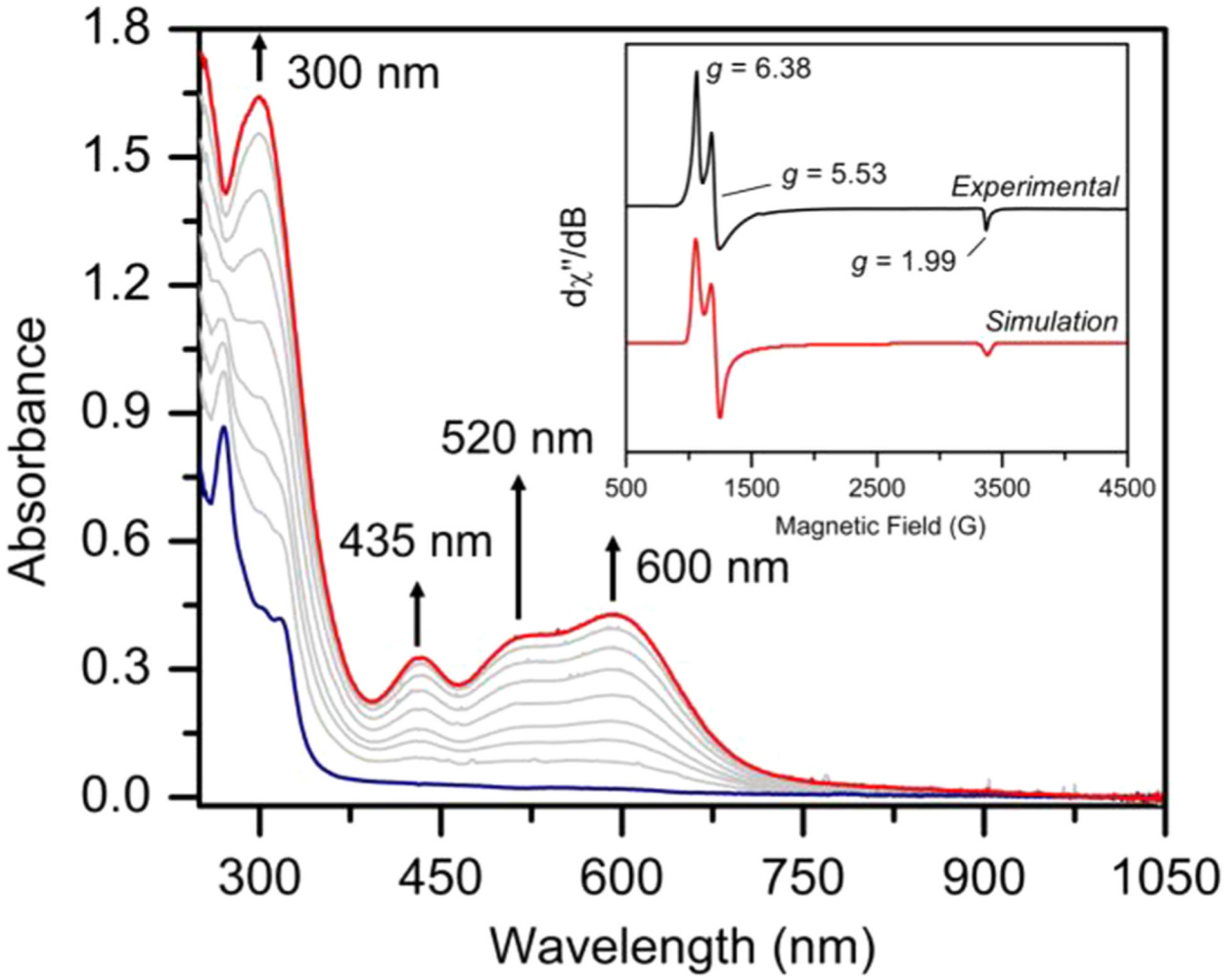

Figure 3.

UV–vis spectral changes for the titration of **1** (0.2 mM) with $^{Me2}FcBAr^{F}_{4}$ (0–1 equiv) in 2-MeTHF at −80 °C. Inset: EPR spectrum of the oxidized species (**1**^{ox}) in 2-MeTHF at 20 K. Black line, experimental data; red line, simulation.

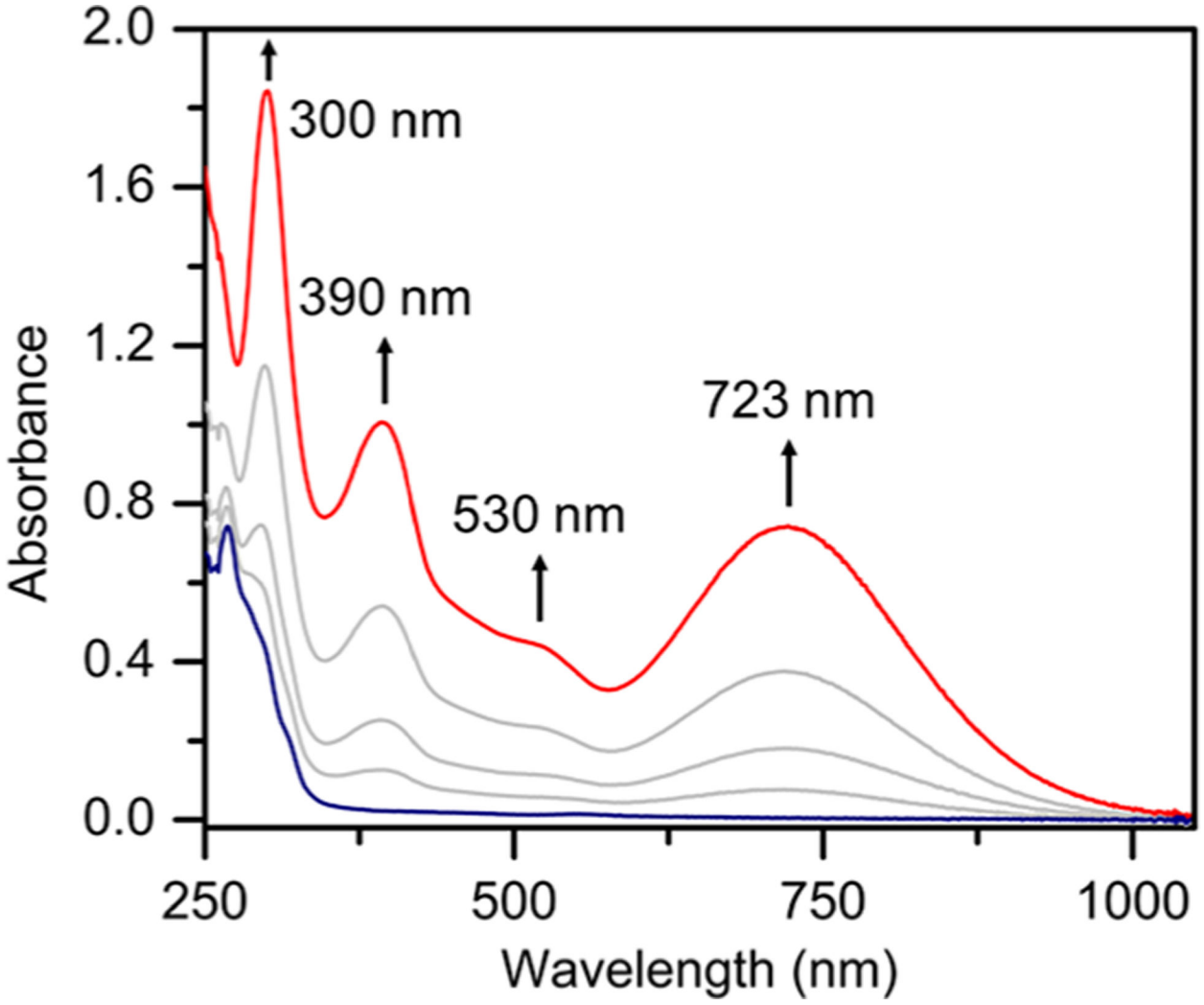

Figure 4.

UV–visible spectra showing conversion of **1** (blue line) (0.2 mM) to **2** (red line) over 5 min of exposure to excess O_2 in 2-MeTHF at −135 °C.

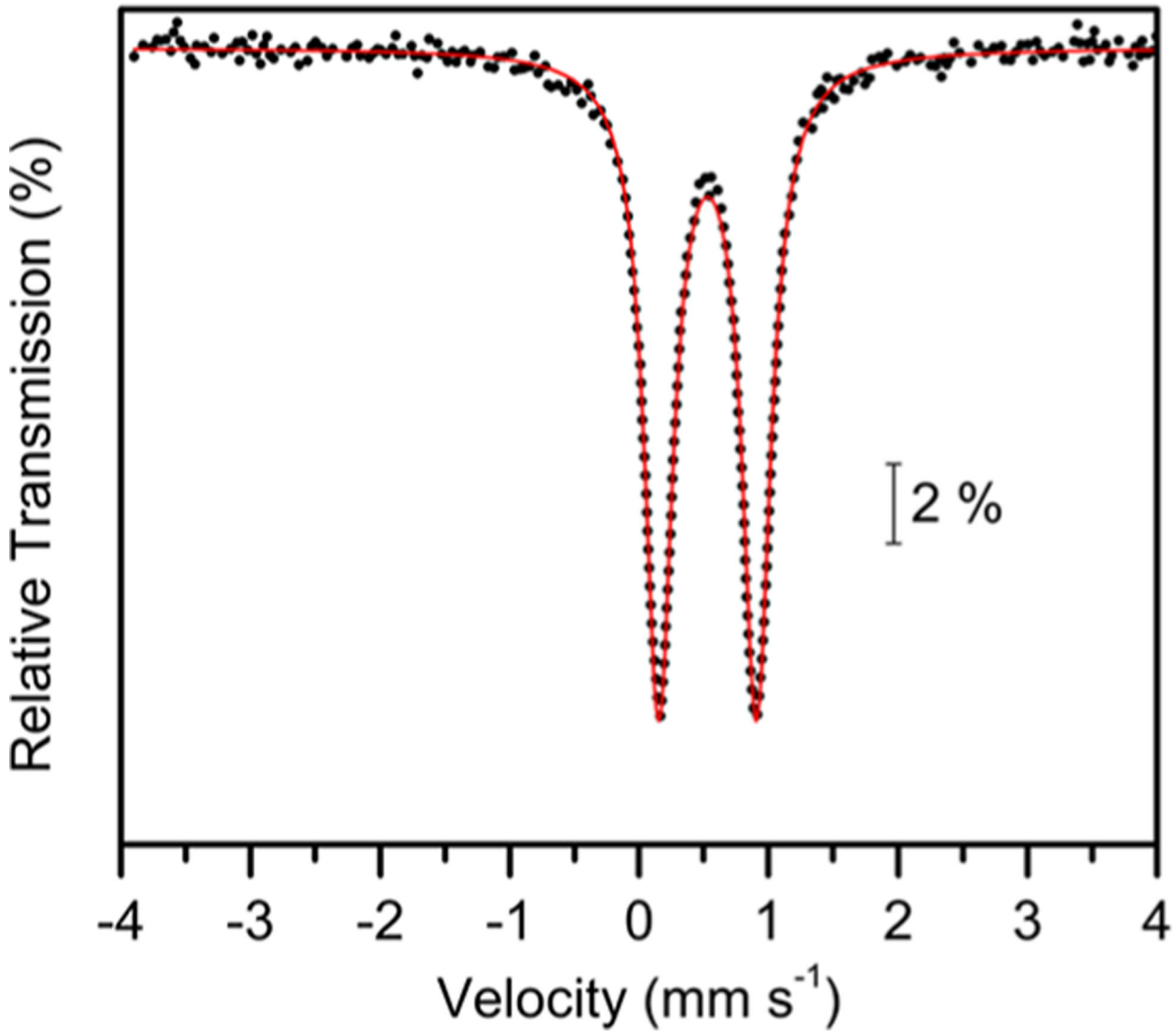

Figure 5.
Zero-field ^{57}Fe Mössbauer spectrum of **2** at 80 K in 2-MeTHF. Fit shown in red.

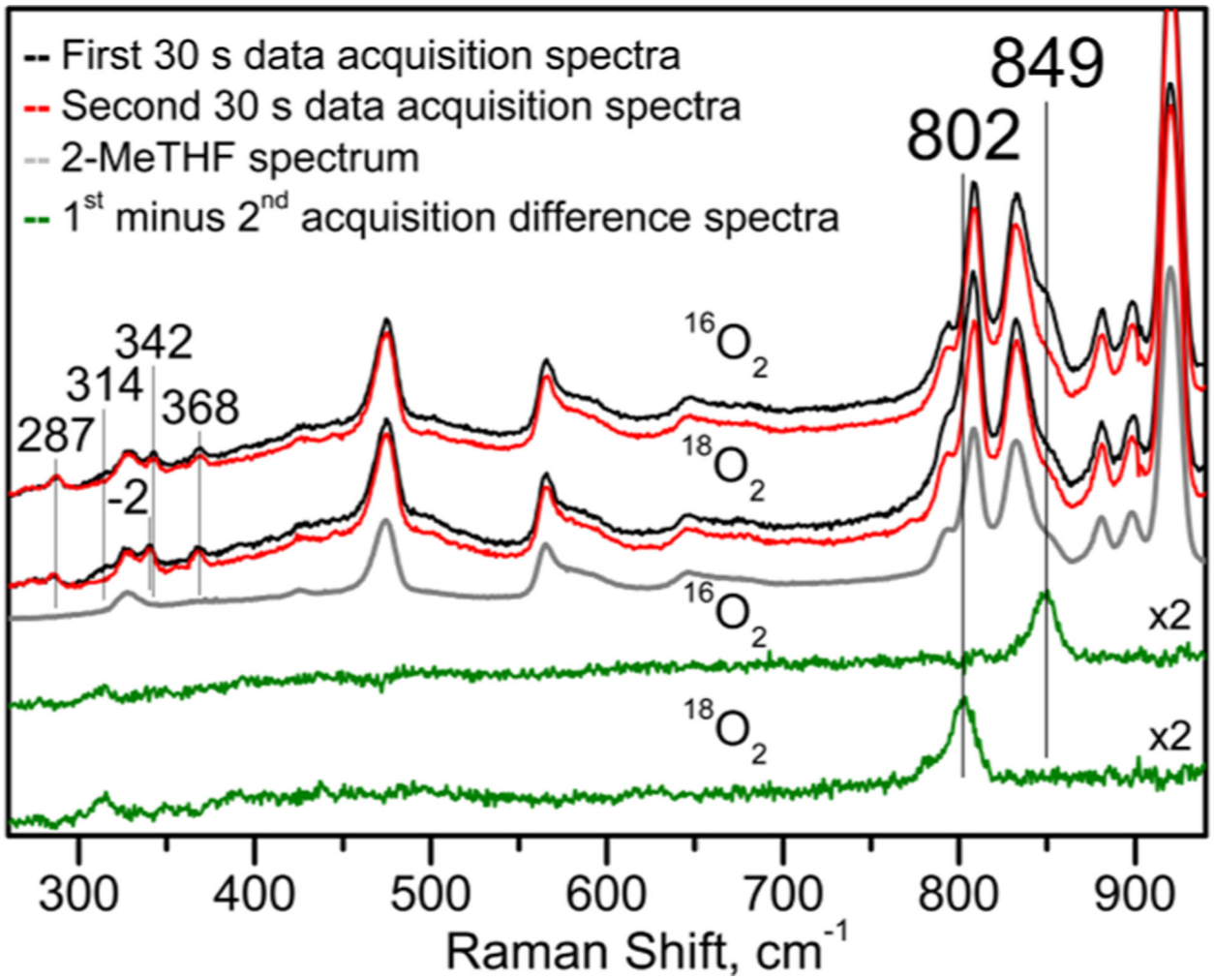

Figure 6.

RR spectra of 2 in 2-MeTHF at 110 K (λ_{exc} = 407 nm). Black and red spectra show first and second 30 s data acquisition, respectively; gray spectrum is that of 2-MeTHF; green spectra are the difference spectra between the first and second 30 s data acquisition sets for samples prepared with $^{16}O_2$ and $^{18}O_2$.

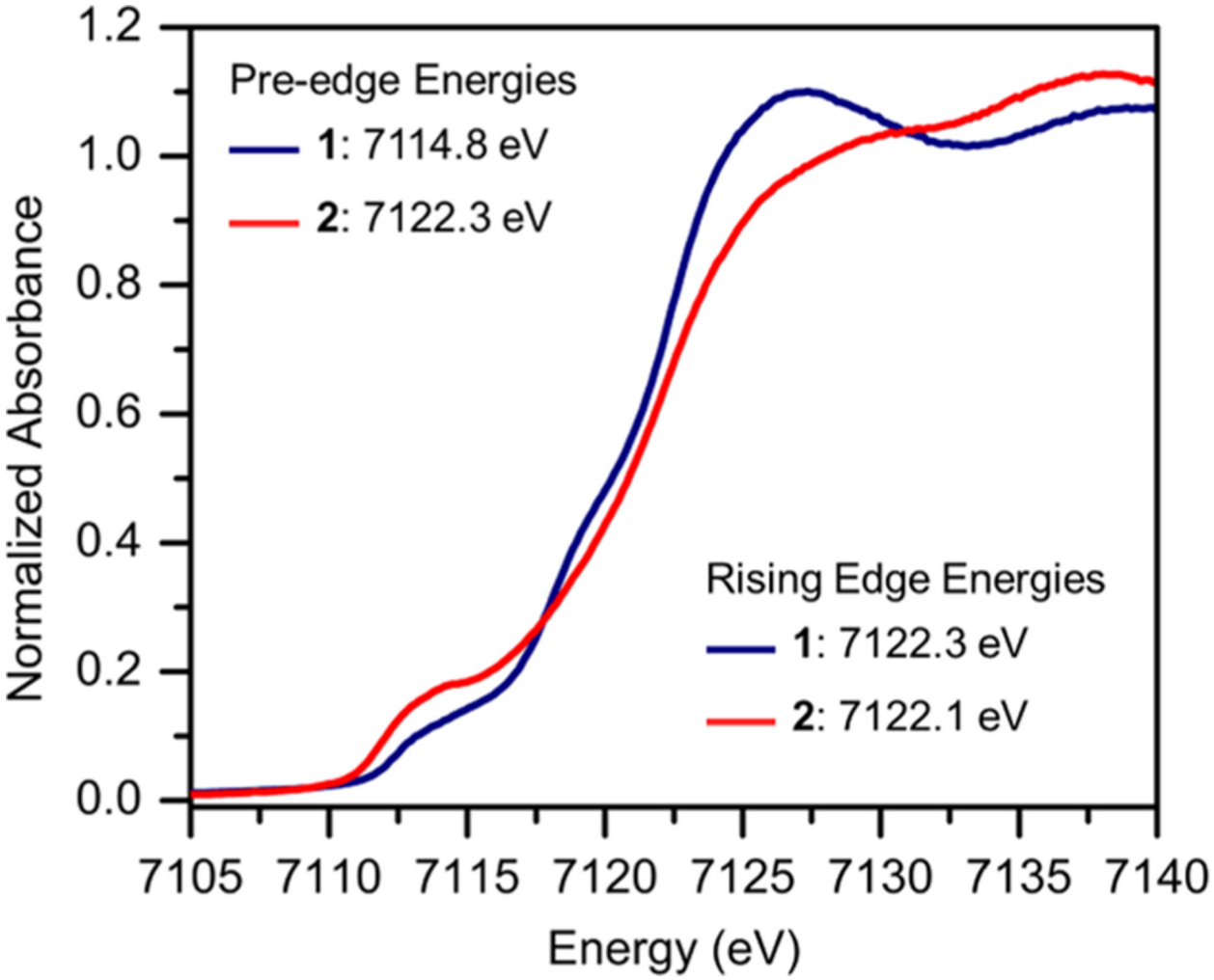

Figure 7.
Fe K-edge XANES data obtained for **1** and **2** at 10 K.

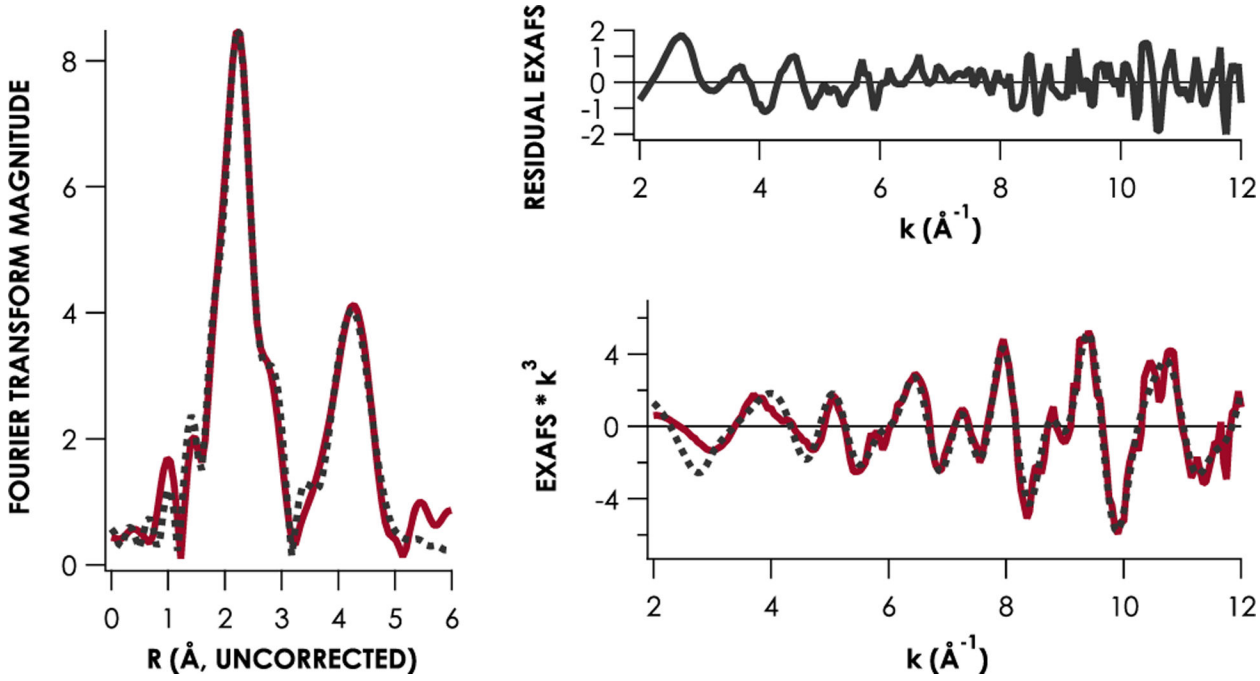

Figure 8.

Fe K-edge EXAFS data obtained for **2** at 10 K. Experimental data are plotted in red, while the dashed line corresponds to the fit obtained using parameters included in Table 1 (entry 11 in Table S2). The Fourier transform includes data from $k = 2–12$ Å^{-1}.

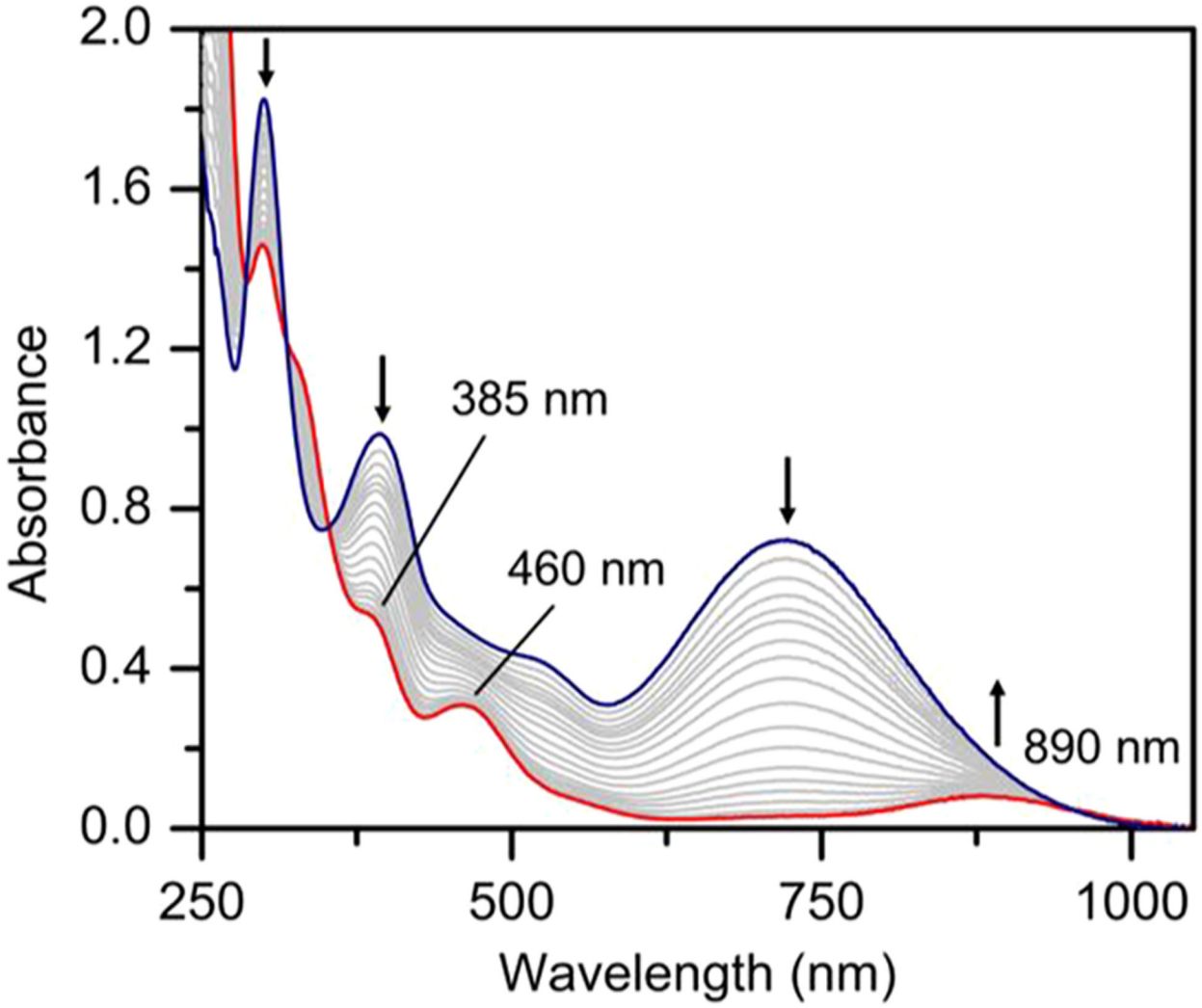

Figure 9.
UV–visible spectra showing conversion of **2** (blue line) to **3** (red line) upon exposure to 619 nm light in 2-MeTHF at −135 °C for 10 min.

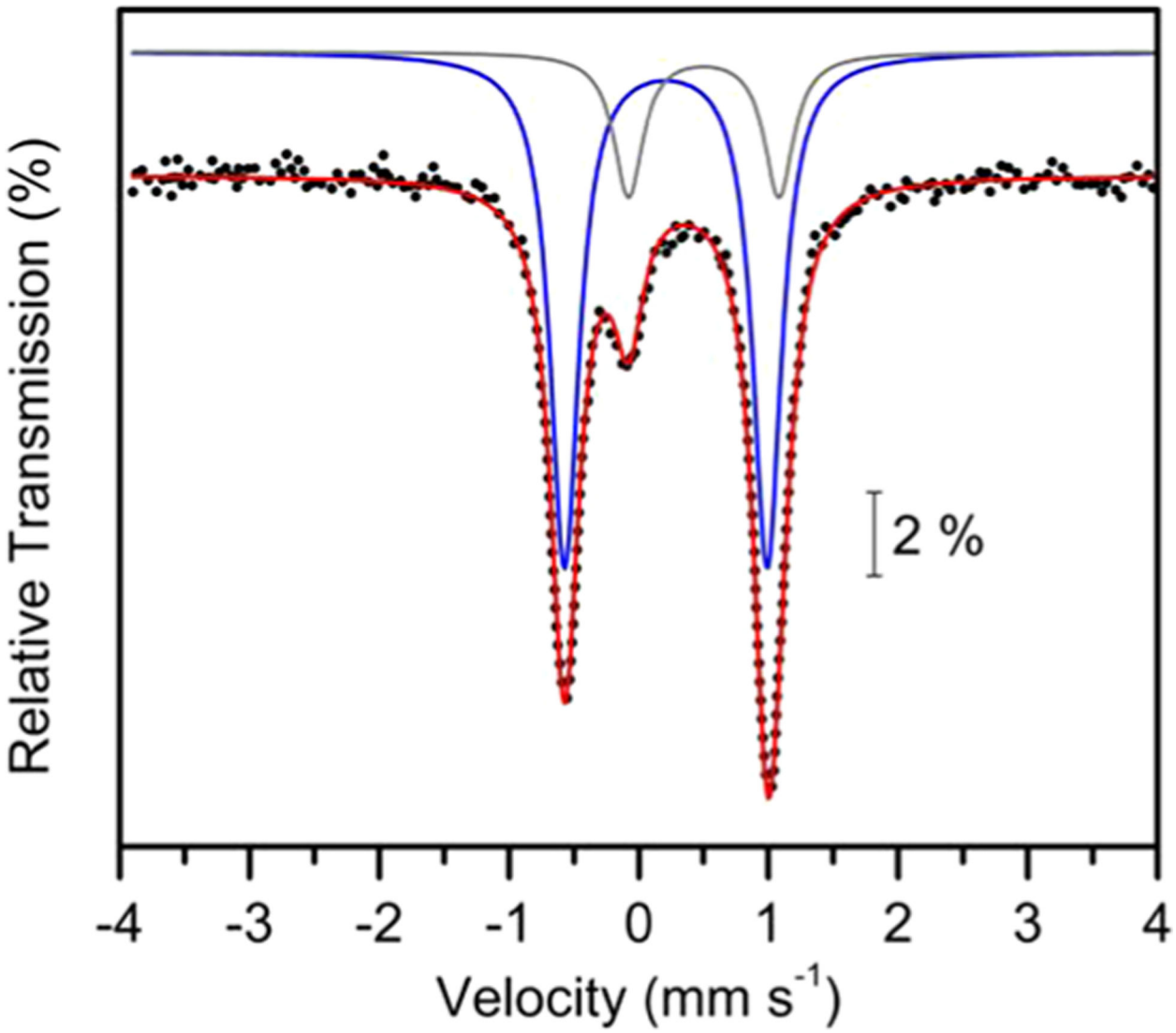

Figure 10.

Zero-field ^{57}Fe Mössbauer spectrum of **3** at 80 K in 2-MeTHF. Overall fit shown as a red line. Fits for subspectra shown as blue and gray lines.

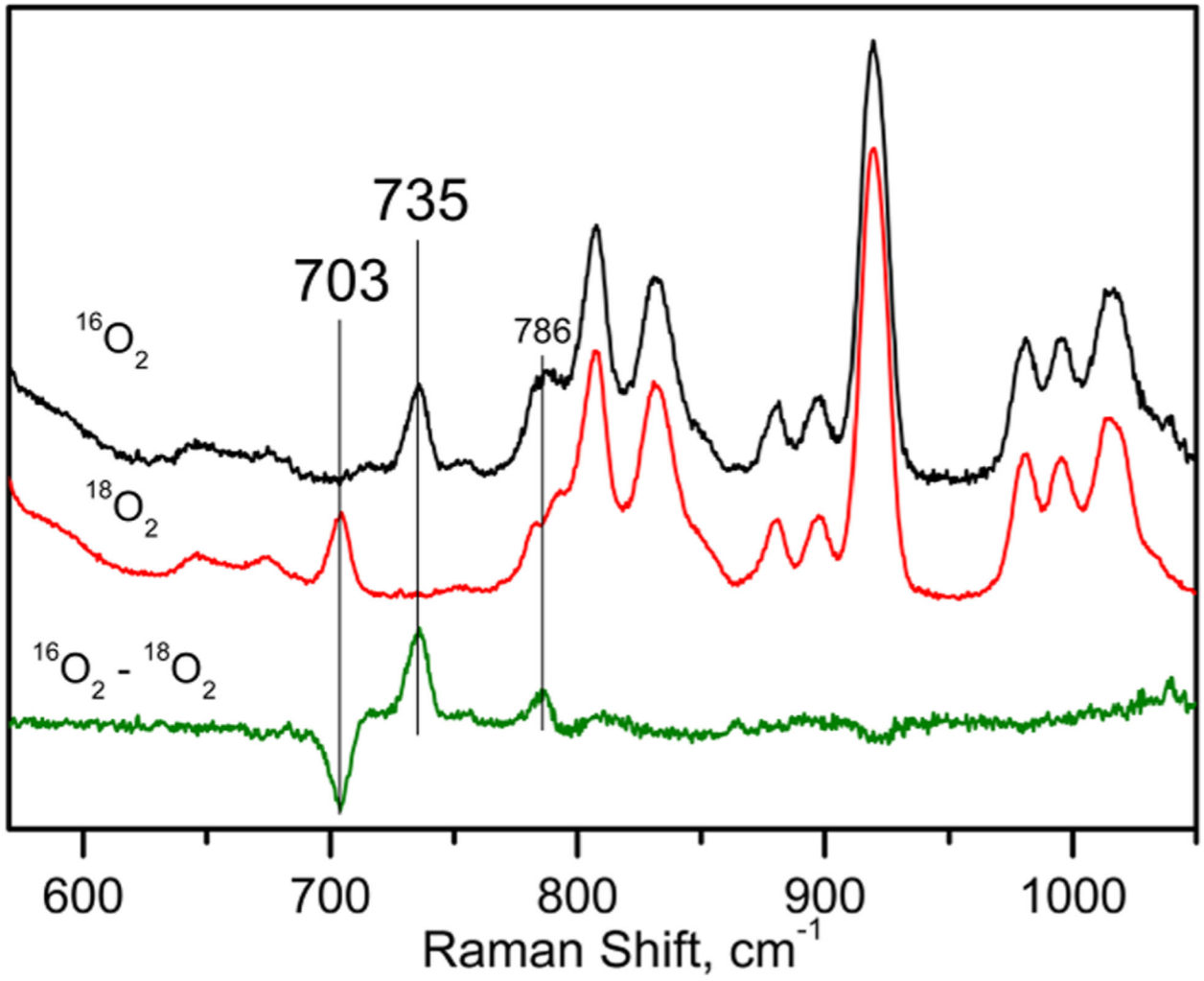

Figure 11.

RR spectra of **3** in 2-MeTHF at 110 K (λ_{exc} = 351 nm). Black spectrum for **3** with $^{16}O_2$ (natural abundance); red spectrum for **3** with $^{18}O_2$ (98%); green spectrum is the difference spectrum ($^{16}O_2$ – $^{18}O_2$).

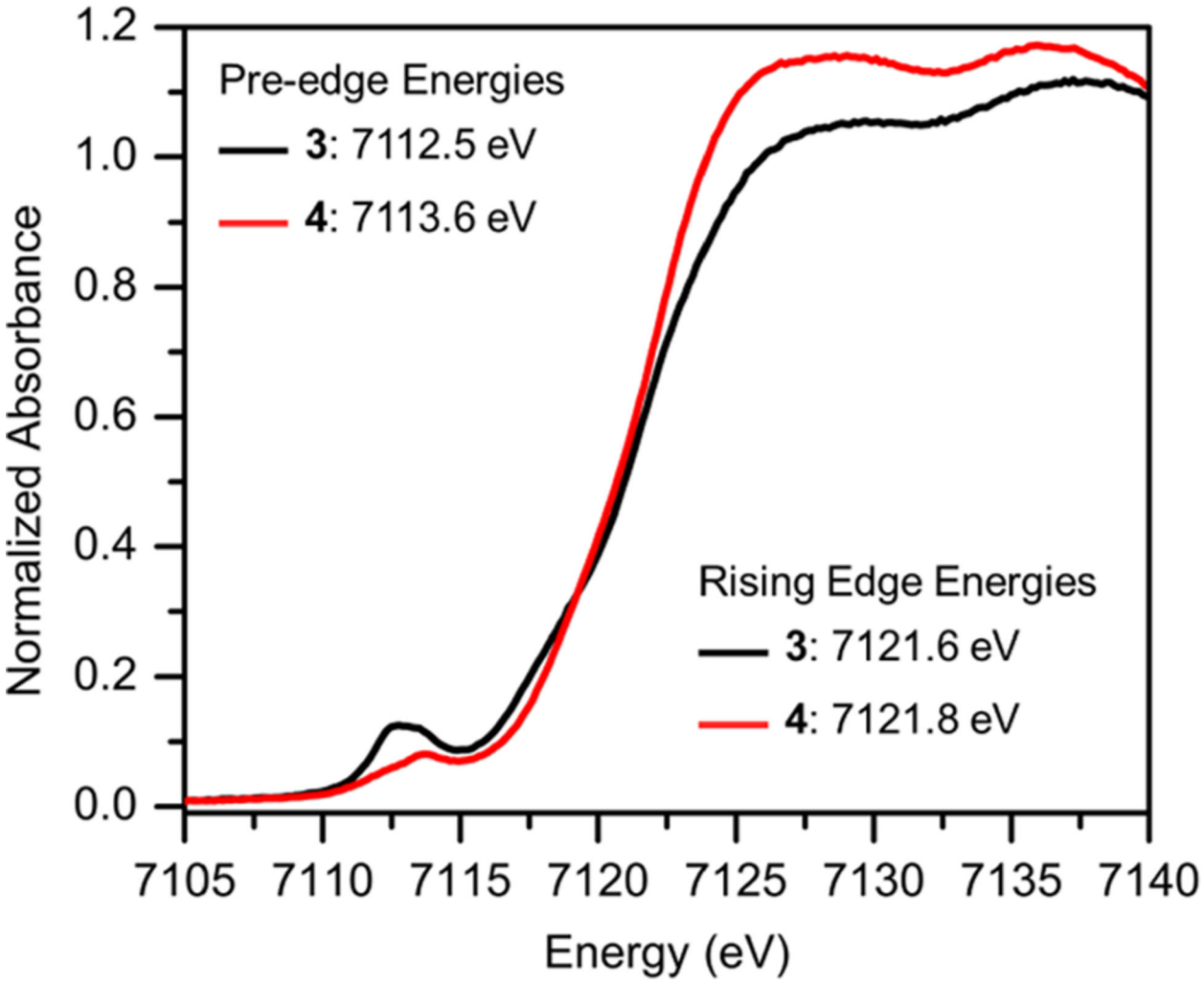

Figure 12.
Fe K-edge XANES data obtained for **3** and **4** at 10 K.

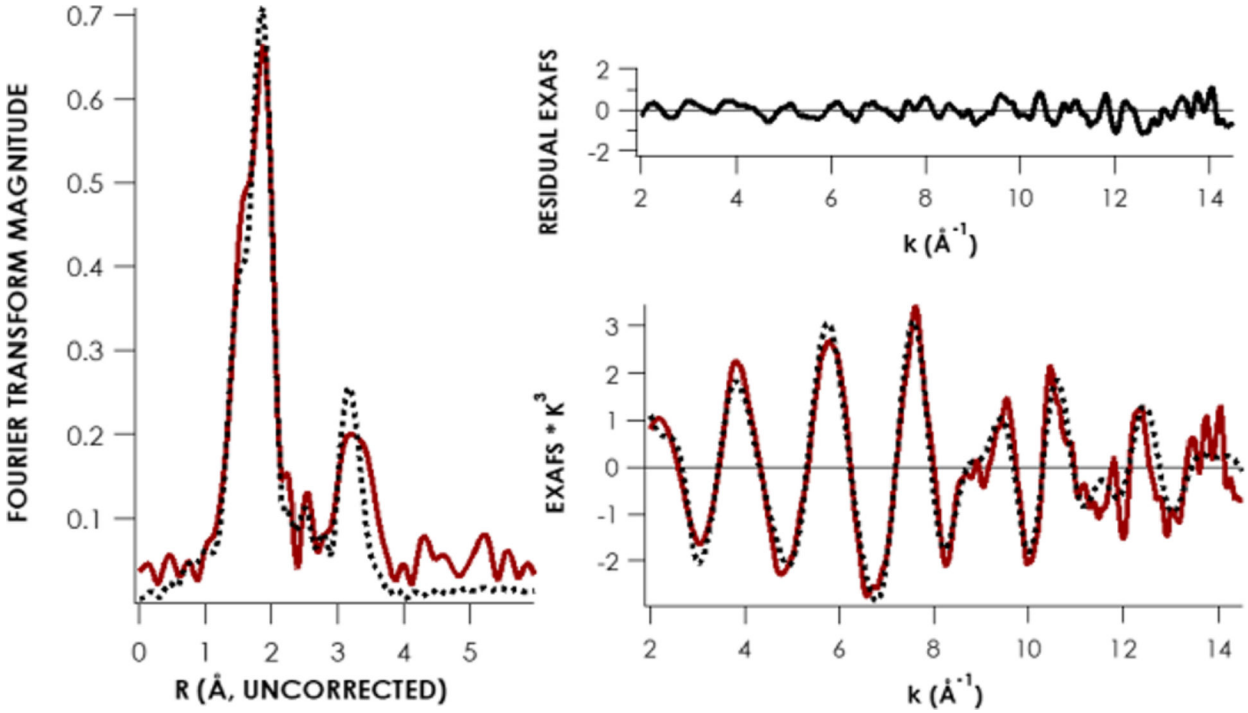

Figure 13.

Fe K-edge EXAFS data obtained for **3** at 10 K. Experimental data are plotted in red, while the dashed line corresponds to the fit obtained using parameters included in Table 2 (entry 8 in Table S3). The Fourier transform includes data from $k = 2–14.4$ Å^{-1}.

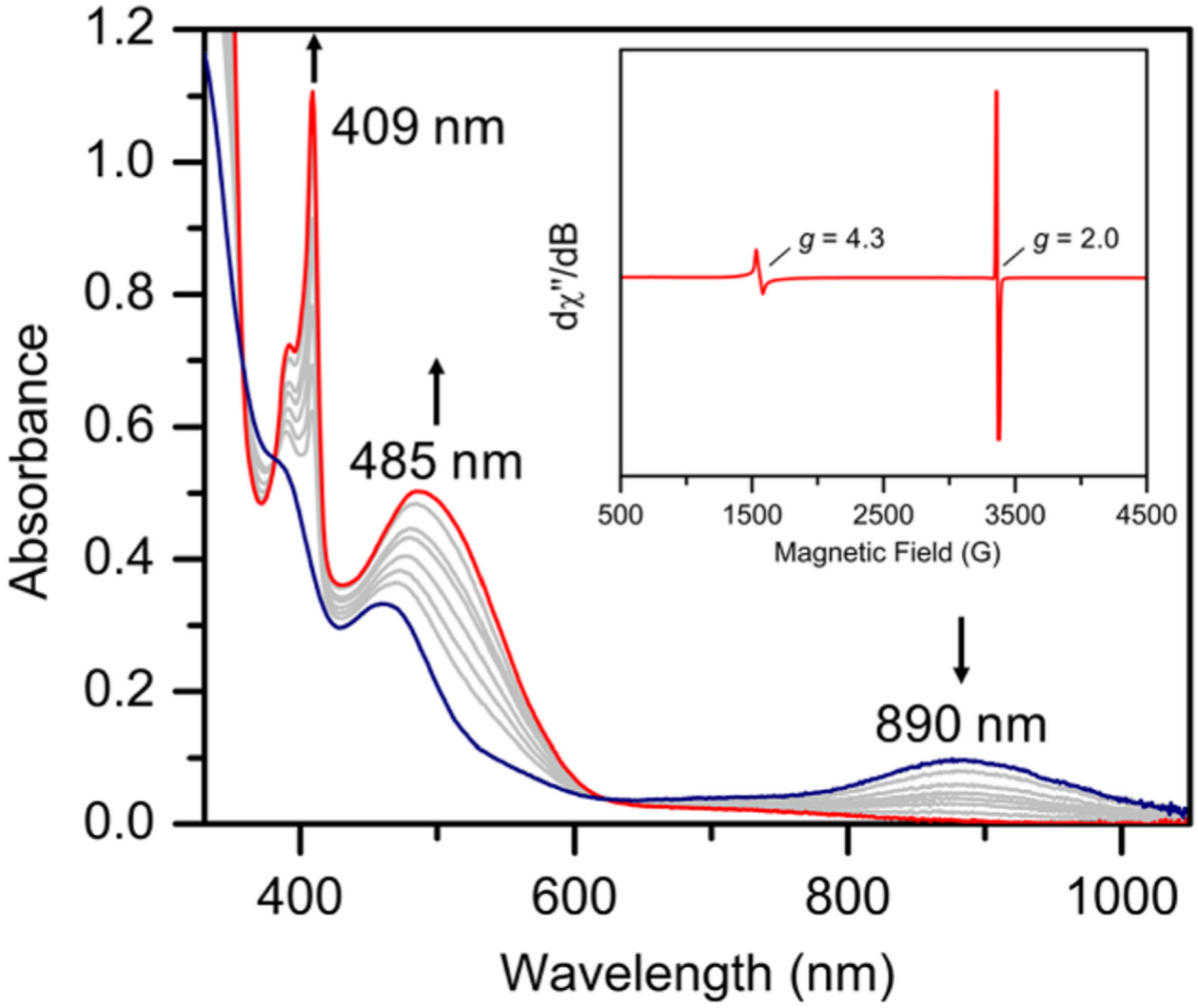

Figure 14.

UV–visible spectra showing reaction of **3** (blue line) (0.2 mM) with 4-OMe-dtbp (9 equiv) 2-MeTHF at −135 °C over 30 min. Inset: X-band EPR spectrum (20 K) of the reaction of **3** (1 mM) with 4-OMe-dtbp in 2-MeTHF. Conditions: Microwave freq = 9.4139 GHz; microwave power = 0.20 mW; mod amp = 10 G; rec gain = 5×10^3.

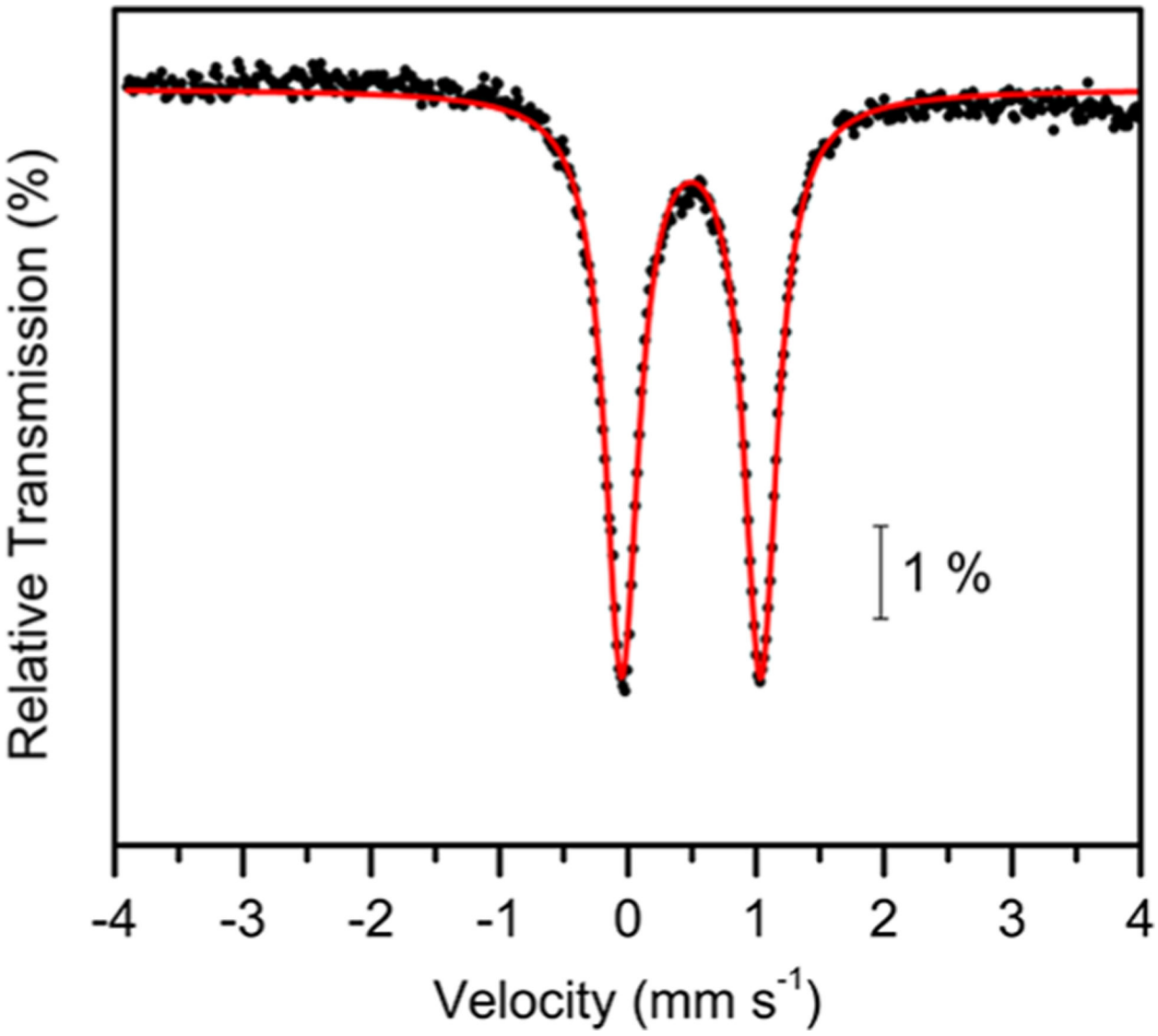

Figure 15.
Zero-field ^{57}Fe Mössbauer spectrum of **4** at 80 K in 2-MeTHF. Fit shown in red.

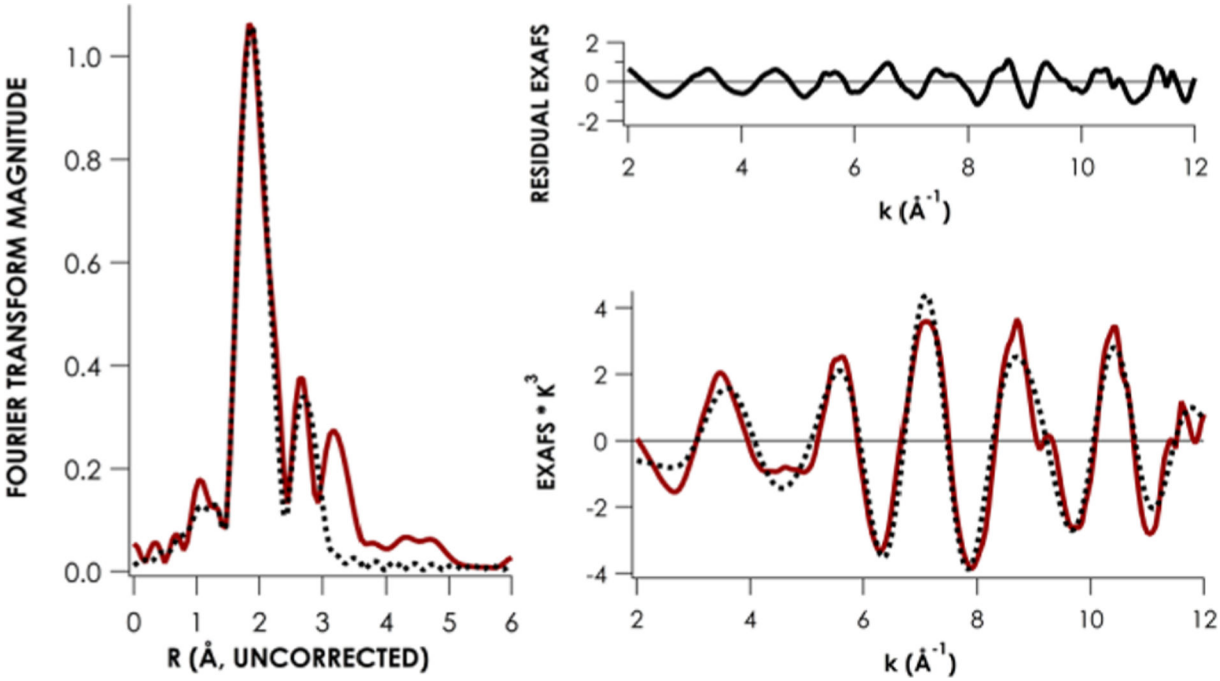

Figure 16.

Fe K-edge EXAFS data obtained for **4** at 10 K. Experimental data are plotted in red, while the dashed line corresponds to the fit obtained using parameters included in Table 3 (entry 5 in Table S4). The Fourier transform includes data from $k = 2–12$ Å^{-1}.

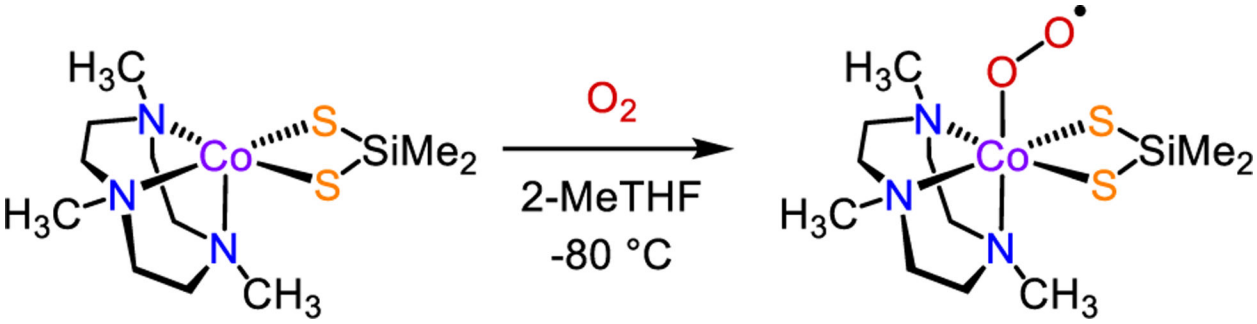

Scheme 1.
Formation of $Co(O_2)(Me_3TACN)(S_2SiMe_2)$

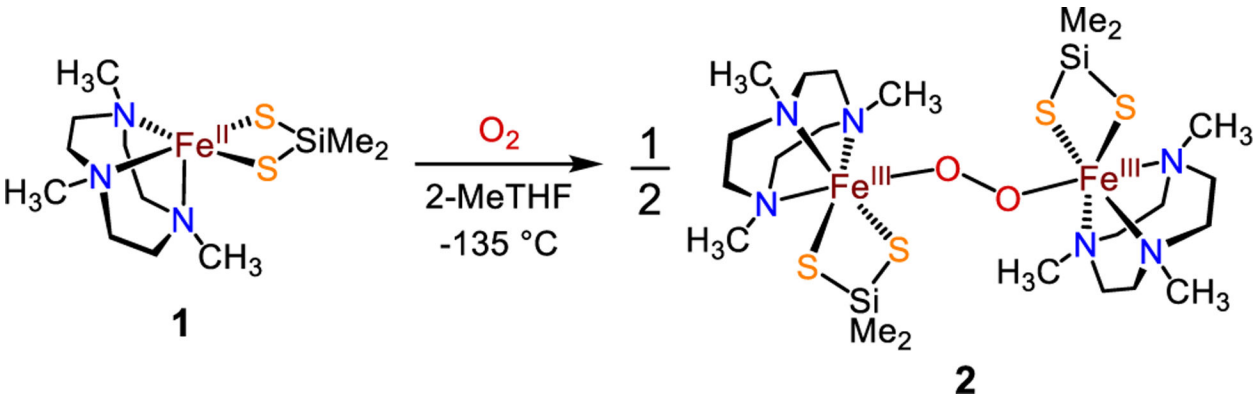

Scheme 2.
Activation of O_2 by Complex 1

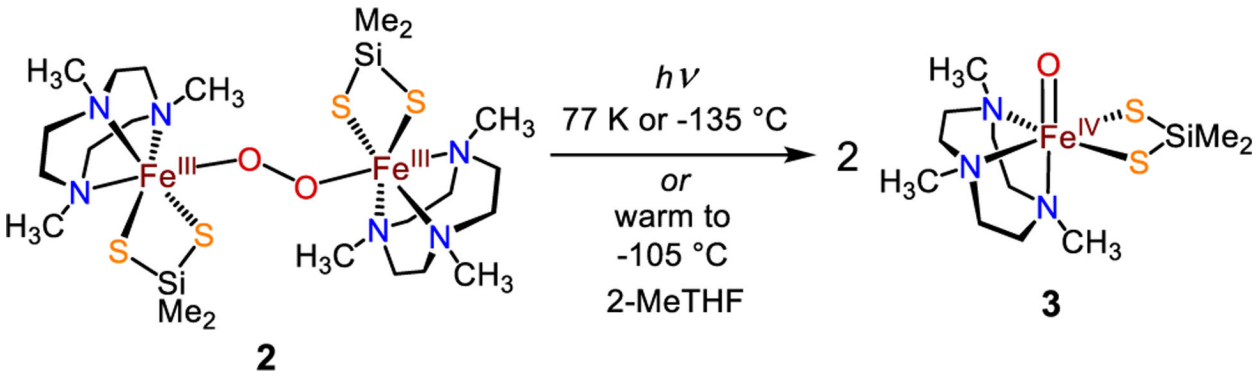

Scheme 3.
O–O Bond Cleavage of Complex 2

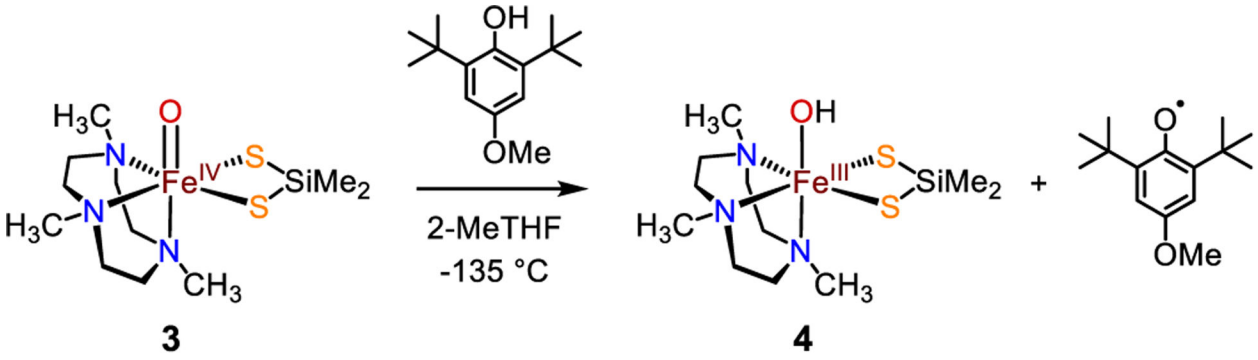

Scheme 4.
Reaction of 3 with an H-Atom Donor

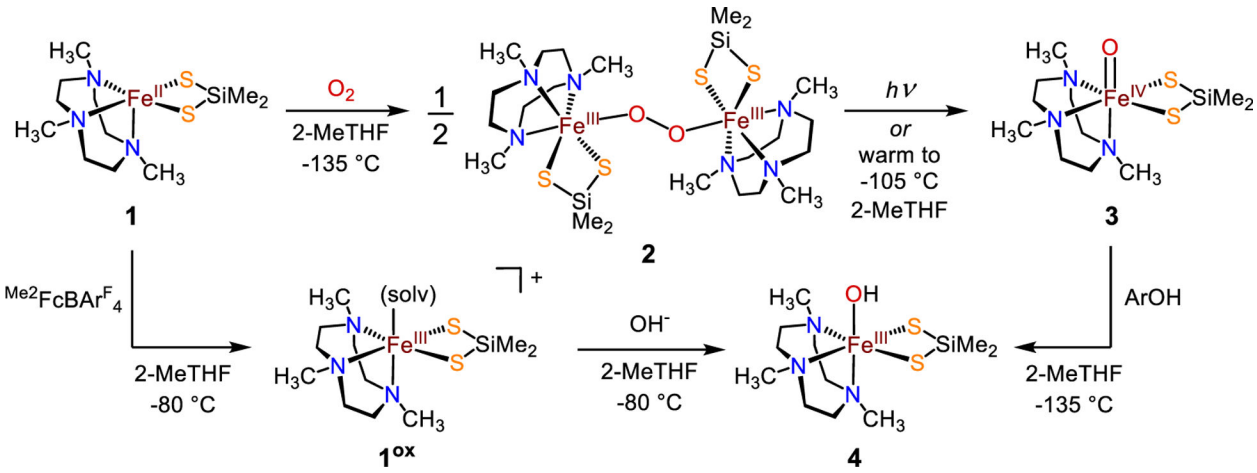

Scheme 5.
Summary of Reactivity of $Fe^{II}(Me_3TACN)(S_2SiMe_2)$

Table 1.

Best Fit to Fe K-Edge EXAFS of Complex 2 (F = 29.81%)[a,b,c]

path	CN	R (Å)	±	σ^2	±
Fe-N	3	2.173	0.007	0.0055	0.0007
Fe-S	2	2.684	0.006	0.0020	0.0004
Fe-O	1	1.931	0.009	0.0029	0.0007
Fe-Fe	1	4.38	0.04	0.010	0.006
Fe-O-Fe (MS)	4	4.740	0.009	0.0047	0.0005
Fe-Si	1	2.91	0.02	0.001	0.001
Fe-N-C (MS)	18	3.37	0.01	0.002	0.002
Fe-C	5	4.09	0.01	0.001	0.001

[a] See Table S2 for a list of sequentially improved fits.

[b] EXAFS data were fit with EXAFSPAK using paths calculated by FEFF7. Coordination numbers (CN) were held constant, whereas distances (R) and Debye–Waller factors (σ^2) were allowed to vary. Goodness of fit was measured with F, which was defined as $\left[\left(\sum_i^n \left[k_i^3(\mathrm{EXAFS_{obs}} - \mathrm{EXAFS_{calc}})_i\right]\right)^2/n\right]^{1/2}$. E_0 for the best fit was +5.15 eV.

[c] Tabulated errors (±) correspond to fitting errors. Expected errors for R are ±0.02 Å; expected errors in CN are ca. 20–25%.[64]

Table 2.

Best Fit to Fe K-Edge EXAFS of Complex 3 (F = 30.25%)[a,b,c]

path	CN	R (Å)	±	σ^2	±
Fe-N	3	2.220	0.003	0.0054	0.0003
Fe-S	2	2.321	0.007	0.022	0.002
Fe-O	0.57(7)	1.687	0.006	0.008	0.001
Fe-N-C	24	3.613	0.004	0.0019	0.0004
Fe-C	2	2.95	0.01	0.007	0.001
Fe-C	4	3.185	0.008	0.0076	0.0009

[a] See Table S3 for a list of sequentially improved fits.

[b] EXAFS data were fit with EXAFSPAK using paths calculated by FEFF7. Coordination numbers (CN) were held constant, whereas distances (R) and Debye–Waller factors (σ^2) were allowed to vary. Goodness of fit was measured with F, which was defined as $\left[\left(\sum_i^n \left[k_i^3(\mathrm{EXAFS_{obs}} - \mathrm{EXAFS_{calc}})_i\right]\right)^2/n\right]^{1/2}$. E_0 for the best fit was +5.15 eV.

[c] Tabulated errors (±) correspond to fitting errors. Expected errors for R are ±0.02 Å; expected errors in CN are ca. 20–25%.[64]

Table 3.

Best Fit to Fe K-Edge EXAFS of Complex 4 (F = 28.75%)[a,b,c]

path	CN	R (Å)	±	σ^2	±
Fe-N	3	2.246	0.018	0.0100	0.0042
Fe-S	2	2.391	0.005	0.0060	0.0011
Fe-OH	1	1.907	0.012	0.0056	0.0010
Fe-N-C	24	3.293	0.011	0.0029	0.0006

[a] See Table S4 for a list of sequentially improved fits.

[b] EXAFS data were fit with EXAFSPAK using paths calculated by FEFF7. Coordination numbers (CN) were held constant, whereas distances (R) and Debye–Waller factors (σ^2) were allowed to vary. Goodness of fit was measured with F, which was defined as $\left[\left(\sum_i^n \left[k_i^3(\mathrm{EXAFS_{obs}} - \mathrm{EXAFS_{calc}})_i\right]\right)^2/n\right]^{1/2}$. E_0 for the best fit was +5.15 eV.

[c] Tabulated errors (±) correspond to fitting errors. Expected errors for R are ±0.02 Å; expected errors in CN are ca. 20–25%.[64]

Table 4.

Summary of Reactivity of $Fe^{II}(Me_3TACN)(S_2SiMe_2)$[a]

complex	UV–vis λ_{max} (nm)	Mössbauer[b] δ; $\lvert\Delta E_q\rvert$ (mm s^{-1})	EPR *g*	RR freq (cm^{-1})	XAS pre-edge; rising edge (eV)
1	269	0.92, 2.27	silent		7114.8; 7122.3
1^{ox}	300, 435, 520, 600	0.45; 3.6	6.38, 5.53, 1.99		
2	300, 390, 530, 723	0.53; 0.76	silent	849 (−47)[c]	7114.7; 7122.1
3	300, 385, 460, 890	0.21; 1.57	silent	735 (−32)[d]	7112.5; 7121.6
4	410, 485	0.49; 1.08	9.3, 4.3		7113.6; 7121.8

[a] All data collected in 2-MeTHF.

[b] Complex **1** collected at 5 K; all other data collected at 80 K.

[c] Frequency refers to ν(O–O), and value in parentheses represents downshift for ^{18}O-labeled complex.

[d] Frequency refers to ν(Fe–O), and value in parentheses represents downshift for ^{18}O-labeled complex.